

1 **High stress deformation and short-term thermal pulse preserved in exhumed lower crustal**
2 **seismogenic faults (Lofoten, Norway)**

3 L. R. Campbell^{1*} & L. Menegon²

4 ¹Department of Geography, Geology and Environment, University of Hull, Hull HU6 7RX

5 ²The Njord Centre, Department of Geosciences, University of Oslo, P.O. Box 1048, Blindern, Norway

6 *Corresponding author email: l.r.campbell@hull.ac.uk

7

8 Key Points

- 9
- 10
- 11
- 12
- 13
- 14
- Localised differential stresses exceeding 1 GPa during pre-seismic loading accommodated in dislocation glide of pyroxenes.
 - Microstructures capable of recording transient stress changes prior to and during seismic rupture in the lower crust.
 - Coseismic deformation represented by pulverisation-style fragmentation and thermally activated grain growth within orthopyroxene.

15

16 **Abstract**

17 Seismic rupture in strong, anhydrous lithologies of the lower continental crust requires high failure
18 stress, in the absence of high pore fluid pressure. Several mechanisms proposed to generate high
19 stresses at depth imply transient loading driven by a spectrum of stress changes, ranging from highly
20 localised stress amplifications to crustal-scale stress transfers. High transient stresses up to GPa
21 magnitude are proposed by field and modelling studies, but the evidence for transient pre-seismic
22 stress loading is often difficult to extract from the geological record due to overprinting by coseismic
23 damage and slip. However, the local preservation of deformation microstructures indicative of
24 crystal-plastic and brittle deformation associated with the seismic cycle in the lower crust offers the
25 opportunity to constrain the progression of deformation before, during and after rupture, including
26 stress and temperature evolution.

27 Here, detailed study of pyroxene microstructures characterises the short-term evolution of high
28 stress deformation and temperature changes experienced prior to, and during, lower crustal
29 earthquake rupture. Pyroxenes are sampled from pseudotachylyte-bearing faults and damage zones
30 of lower crustal earthquakes recorded in the exhumed granulite facies terrane of Lofoten, northern
31 Norway. The progressive sequence of microstructures indicates localised high-stress (at the GPa
32 level) preseismic loading accommodated by low temperature plasticity, followed by coseismic
33 pulverisation-style fragmentation and subsequent grain growth triggered by the short-term heat
34 pulse associated with frictional sliding. Thus, up to GPa-level transient high stress leading to
35 earthquake nucleation in the dry lower crust can occur in nature, and can be preserved in the fault
36 rock microstructure.

37

38 Plain language summary

39 Earthquake initiation within strong, dry rock types in the lower continental crust requires high
40 driving stresses, if fluids are absent. There are several methods proposed to generate these
41 unusually high stresses at lower crustal depths, many implying very short-term stress increases. High
42 short-term stresses up to GPa magnitudes are proposed by the results of fieldwork and numerical
43 modelling, but the geological record for these stress increases occurring in the build-up to
44 earthquakes is not always clear due to the subsequent earthquake deformation overwriting any
45 previous microstructures. However, locally, a complete record of stress change before, during and
46 after an earthquake may be preserved.

47 Here, a detailed study of pyroxene deformation microstructures characterises the short-term
48 changes in stress and temperature experienced prior to, and during, lower crustal earthquakes.
49 Pyroxene crystals close to faults exhibiting ancient earthquake-generated frictional melts
50 (pseudotachylytes) are investigated from an exhumed shear zone in Lofoten, northern Norway. The
51 microstructures imply high stress loading prior to the earthquake, followed by pervasive
52 fragmentation and subsequent grain growth linked to the passage of the earthquake rupture. These
53 results support GPa magnitude stresses localised in the lower crust and show that microstructures
54 are capable of preserving these short term changes.

55 1. Introduction

56 Relocations of focal mechanisms and increased recognition of the geological signature of
57 earthquakes recorded in exhumed lower crustal terranes have promoted the exploration of a
58 number of models for nucleating seismic rupture within otherwise typically viscous deformation
59 regimes. Many of these models require stress amplification or transfer, whether driven by local
60 rheological heterogeneities across a shear zone network (Orlandini & Mahan, 2020; Campbell *et al.*
61 2020, Hawemann *et al.* 2019), dehydration reactions that increase fluid pressure (Hacker *et al.*,
62 2003) or locally redistribute stress (Ferrand *et al.*, 2017), or downdip stress loading from seismogenic
63 activity shallower in the crust (Jamtveit *et al.*, 2018; Dunkel *et al.*, 2020; Papa *et al.*, 2020; Ellis &
64 Stöckhert, 2004). Intracrystalline deformation and recrystallisation occurring over geologically rapid
65 timescales (i.e. equivalent to the seismic cycle) has been previously recognised in fault zones and
66 deformation experiments (Bestmann *et al.*, 2012; Campbell & Menegon, 2019; Kidder *et al.*, 2016),
67 and recent work on both naturally and experimentally deformed mid- to lower- crustal rocks has
68 linked similar microstructures to transient variations in stress. In some cases, such microstructures
69 can be clearly linked to localised stress amplifications associated with deep crustal earthquakes,
70 whether stress increases were generated in-situ within the lower crust (Anderson *et al.*, 2021;
71 Campbell *et al.* 2020; Hawemann *et al.*, 2019) or were transferred from shallower crustal levels
72 (Papa *et al.*, 2020; Ellis & Stöckhert, 2004; Trepmann & Stöckhert, 2013; Trepmann & Stöckhert,
73 2002). In both cases the stress amplification can be significant (e.g. 100s MPa, Ellis & Stöckhert
74 2004), but earthquake nucleation in the lower crustal may require stresses on the order of GPa,
75 especially within strong, anhydrous granulite terranes in the absence of high pore fluid pressure.
76 Such stress magnitudes have recently been captured in mica kink-bands linked to pre-seismic stress
77 accumulation (Anderson *et al.* 2021) and implied by field characterisation of pseudotachylyte-
78 bearing faults (Campbell *et al.*, 2020). The ability of microstructures to capture progressive and
79 transient stress variation throughout the earthquake cycle (Brückner & Trepmann, 2021; Anderson
80 *et al.*, 2021, Campbell & Menegon, 2019, Petley-Ragan *et al.*, 2019) offers an under-explored
81 opportunity to further investigate deformation mechanisms and conditions associated with stress
82 amplification and rupture in the lower crust.

83 We present here a microstructural study of lower crustal pseudotachylyte-bearing faults that seeks
84 to constrain the timing and magnitude of stresses associated with the nucleation and propagation of
85 seismic rupture in the lower crust, as well as the corresponding sequence of deformation processes.
86 Following work on deformation of plagioclase (e.g. Soda and Okudaira, 2018; Petley-Ragan *et al.*,
87 2018, 2021) and garnet (Austrheim *et al.*, 2017; Petley-Ragan *et al.*, 2019; Hawemann *et al.*, 2019;

88 Papa et al., 2018) in lower crustal seismogenic faults, we focus on the deformation microstructures
89 of pyroxenes, which present a clearer record relative to plagioclase of overprinting and spatial
90 association of deformation with localised faulting in our samples. By studying orthopyroxene and
91 clinopyroxene both from the margins of, and as unmelted survivor clasts within granulite-facies
92 pseudotachylyte-bearing faults, we are able to propose a record of spatial and temporal stress and
93 temperature variation related to the seismic cycle in the lower continental crust.

94

95 2. Geological context

96 We investigate pseudotachylyte samples from the Flakstadøy anorthosite near Nusfjord, Lofoten,
97 Norway. This anorthosite body forms part of the Anorthosite-Mangerite-Charnockite-Granite
98 (AMCG) suite, intruded into the lower crust of the Baltic Shield around 1.9-1.7 Ga at granulite facies
99 conditions (Corfu, 2004). The well-preserved coarse-grained igneous texture and mineralogy of the
100 Flakstadøy anorthosite consists of plagioclase + minor amounts of clinopyroxene ± amphibole ±
101 quartz ± orthopyroxene ± garnet ± biotite (Markl et al., 1998; Menegon et al., 2017). The anorthosite
102 can be considered anhydrous, containing ca. 0.04 wt. % H₂O and no free H₂O at the time of
103 deformation (Menegon et al., 2017).

104 Within the Flakstadøy anorthosite, a network of thin shear zones (usually 1 – 30 cm in width) cut
105 across the intrusion, occurring in three dominant orientations (Menegon et al., 2017) and dividing up
106 the anorthosite into a series of low strain blocks (Fig. 1a). In turn, these blocks are cut by
107 pseudotachylyte-bearing faults (Fig. 1b), indicating episodic seismic failure ('type-2'
108 pseudotachylytes of Campbell et al., 2020). The surrounding anorthosite, whilst fractured, also
109 typically shows very limited evidence of viscous creep away from either the shear zones or the
110 pseudotachylyte veins (Fig. 1c). The transient high stresses required to trigger seismic failure within
111 these blocks were interpreted to result from localised stress amplifications driven by activity along
112 the viscously deforming shear zones (Campbell et al., 2020). Therefore, the seismicity recorded by
113 these 'type-2' pseudotachylytes nucleated at ambient conditions of the coeval shear zone
114 deformation, 650-750 °C and 0.7-0.8 GPa (Menegon et al., 2017), implying depths of 25 – 30 km in
115 the continental lower crust. These 'type-2' pseudotachylyte veins (Fig. 1d) show very limited
116 overprinting by viscous reactivation, preserving primary quench crystallisation morphologies (e.g.
117 radiating microlites, spherulites, dendritic crystals) and chilled margins (Fig. 1d, e). In this
118 contribution, we look for the microstructural evidence to constrain potential GPa levels of
119 preseismic loading suggested by Campbell et al. (2020), and identify further coseismic rapid stress
120 and temperature oscillations.

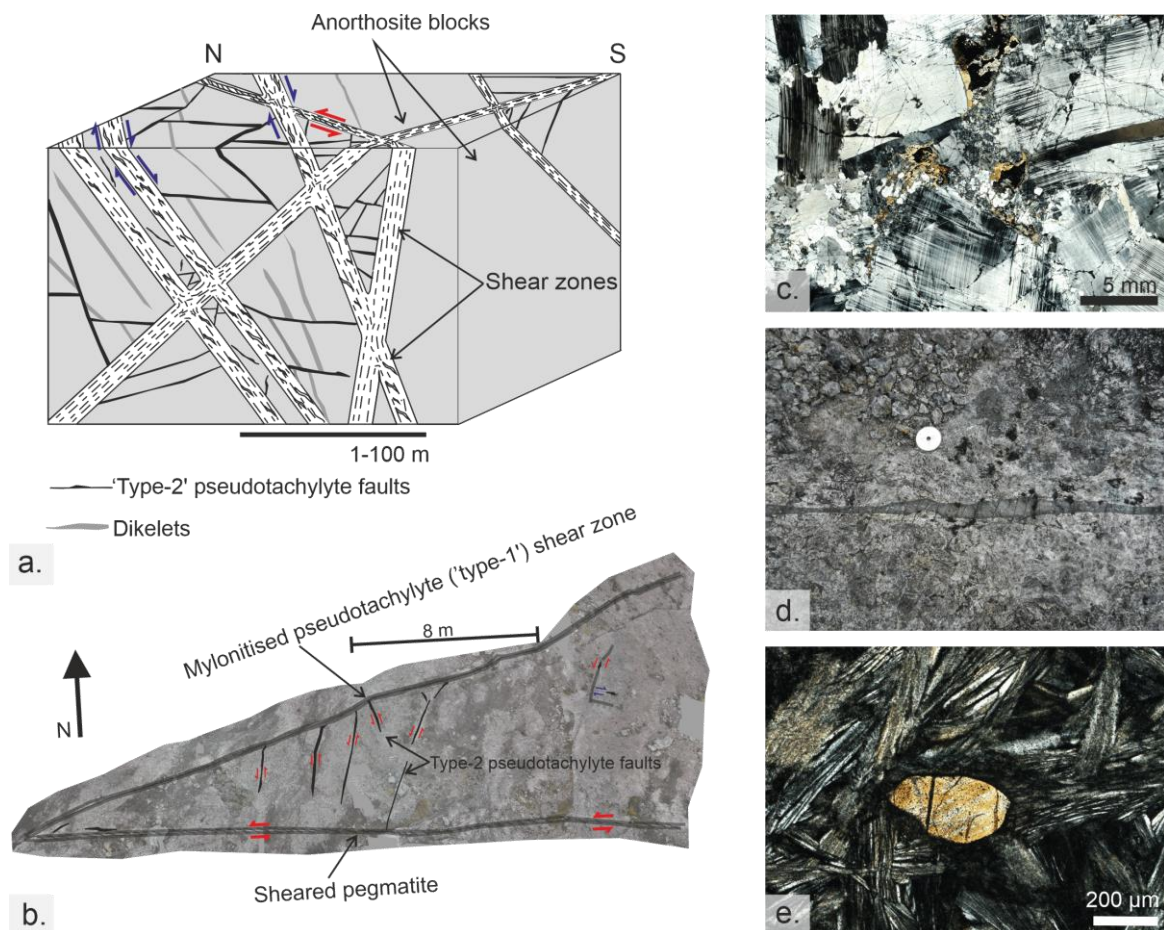


Figure 1. Pseudotachylytes representing lower crustal earthquake nucleation associated with viscous creep along active shear zone networks near Nusfjord, Lofoten. **a)** Block diagram showing pseudotachylyte faults that dissect low-strain anorthosite blocks between localised viscous shear zones; **b)** map of faults and shear zones across one such block in the Flakstadøy anorthosite (68.055°N 13.367°E); **c)** typical form of anorthosite within shear-zone bounded blocks at distance from pseudotachylyte faults (cross-polarised image). **d)** example of pseudotachylyte fault with chilled margin, located in block shown in b) (68.055°N 13.367°E); **e)** Orthopyroxene clast in crystalline matrix of pseudotachylyte showing characteristic radiating plagioclase microlites (cross-polarised image).

121 3. Methods

122 3.1 Microstructural analysis and electron backscatter diffraction (EBSD)

123 Polished thin sections of samples of pseudotachylyte veins were cut perpendicular to the vein wall
 124 but the slip directions remain unconstrained. Thin sections were analysed using a combination of
 125 light and scanning electron microscopy (SEM). SEM data were acquired at the Electron Microscopy
 126 Centre at the University of Plymouth using a JEOL 7001 FEG-SEM and a JEOL 6610 low vacuum SEM.
 127 Typical beam conditions were 10-13 nA probe current and 20 kV accelerating voltage.

128 Samples for electron backscatter diffraction (EBSD) analysis underwent additional preparation with
 129 colloidal silica polishing and carbon coating. Data were acquired at the Electron Microscopy Centre
 130 at the University of Plymouth using a JEOL 7001 FEG-SEM and a JEOL 6610 low vacuum SEM,
 131 equipped with an Oxford Instruments Nordlys Nano and a Nordlys Max detector, respectively.
 132 During EBSD analysis, working distances were set up between 15.2 mm and 24.2 mm, accelerating

133 voltage was 20 kV and the sample was tilted at 70°. Step sizes for EBSD mapping ranged from 0.1 μm
134 to 0.9 μm . Phases were indexed using AZtec (Oxford Instruments) acquisition software. Processing
135 was undertaken with Channel 5 (Oxford Instruments) software. Filtering of the raw data involved
136 removing wild spikes, nearest neighbour extrapolation and removal of any grains with circle-
137 equivalent diameters less than three times the step size. The results are presented in the form of
138 phase maps, orientation maps (inverse pole figure, IPF, maps), grain orientation spread (GOS) maps,
139 showing the average misorientation of a grain with respect to that grain's mean orientation, grain
140 reference orientation deviation (GROD) maps, showing the misorientation of points relative to that
141 grain's mean orientation, and texture component (TC) maps showing the misorientation with
142 respect to a chosen point in a given grain. Pole figures (lower hemisphere, equal angle) and maps are
143 orientated with respect to the pseudotachylyte vein and pole figures show a reference frame
144 perpendicular (Z_v) and parallel (X_v) to the vein edge.

145 3.2 Boundary trace analysis

146 Identification of slip systems using EBSD analysis was undertaken using the boundary trace analysis
147 (BTA) technique. Using this method, subsetted regions transecting low-angle boundaries (with
148 misorientation in the 2-9° range) were created from EBSD orientation maps. Pole figures were
149 created for each subset. The BTA method assumes a tilt boundary model, where the two regions
150 each side of the boundary are rotated around an axis parallel to the boundary plane. This axis,
151 providing it is parallel to a crystal axis, will be represented in the pole figure by a tight point cluster
152 at the position of that axis, whilst the other crystal axes may show rotation around that orientation
153 via a dispersed smear of points. The slip plane can be identified as it must contain both the rotation
154 axis and the slip direction, and the slip direction along with the pole to the slip plane must lie in a
155 plane that is perpendicular to the rotation axis (Lloyd et al., 1997).

156 3.3 Image analysis for grain size distributions

157 Analysis of grain size distributions of fine-grained pyroxene aggregates occurring in the damage zone
158 of and in survivor clasts within type-2 pseudotachylytes was undertaken using the freely available
159 image analysis software 'ImageJ'. Grain boundaries were identified via segmentation of SEM
160 backscatter electron (BSE) images acquired at magnification ranging from 850x to 2300x. Grain area
161 and circle equivalent diameter (D_{equ}) were then measured and calculated with ImageJ.

162 4. Results

163 4.1 Sample description

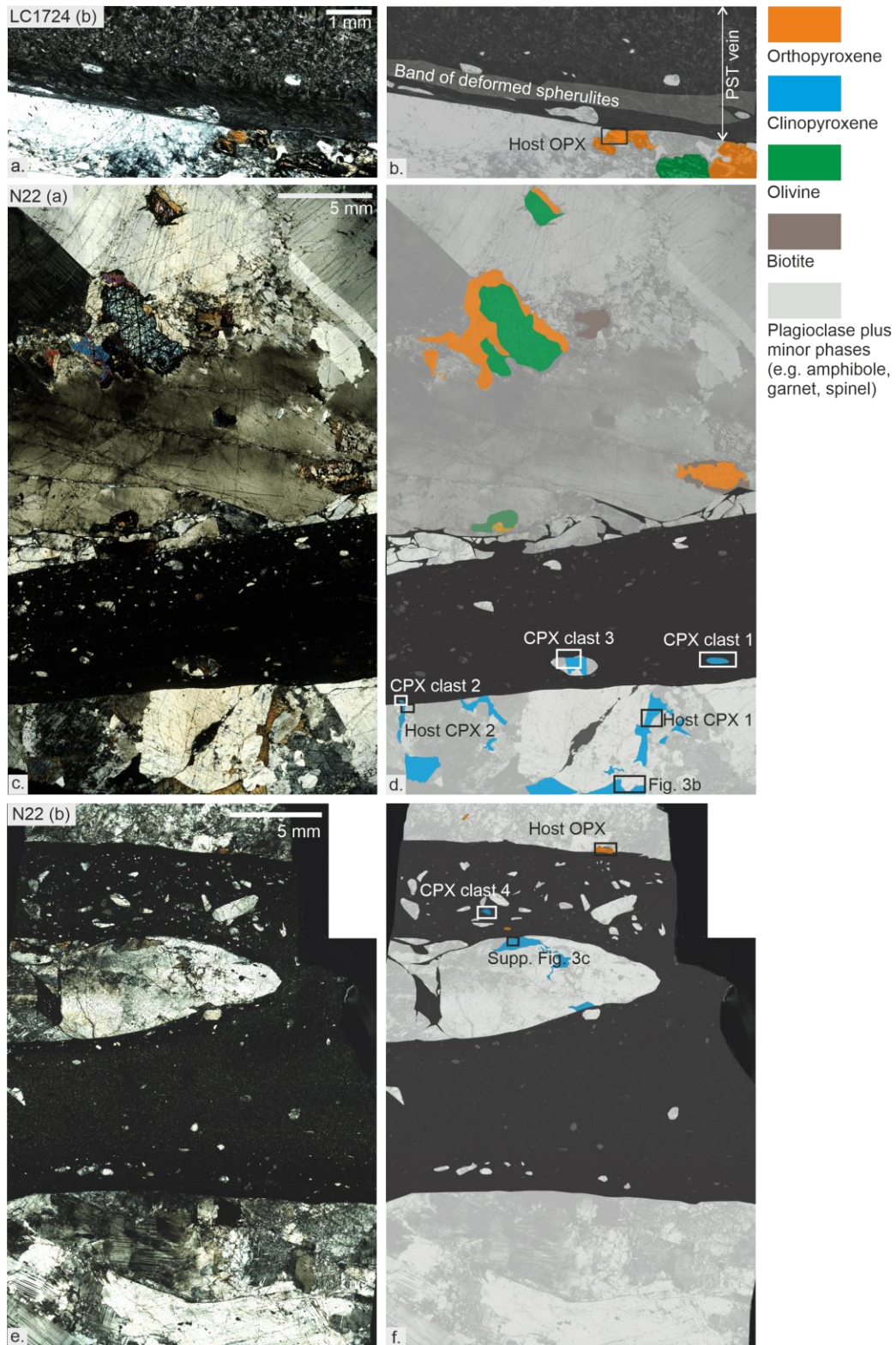


Figure 2. Distribution of pyroxenes and other phases in association with pseudotachylyte veins (blue = clinopyroxene; orange = orthopyroxene; green = olivine). Areas analysed in this work are labelled; **a)** pseudotachylyte fault vein and anorthosite host rock in sample LC1724. (Only one side of the fault is captured – the margin of this pseudotachylyte vein has a 1 mm thick band of sinistrally sheared spherulitic structures (cross-polarised light, thin section ‘b’); **b)** overlay highlighting mineralogy of a); **c)** pseudotachylyte fault vein cutting anorthosite in sample N22 (cross-polarised light, thin section ‘a’); **d)** overlay highlighting mineralogy in c); **e)** Thin section N22b (cross-polarised light) showing pseudotachylyte vein and clasts; **f)** overlay showing mineralogy of e).

164 Pyroxenes are described from two pseudotachylyte veins: LC1724 (Figs. 2a-b) and N22 (Figs. 2c-f).

165 These veins consist of pristine, unaltered pseudotachylyte that preserves quench crystallisation
166 morphologies of the coseismic melt, such as chilled margins, radiating microlites and spherulites
167 (Figs. 1e, 2). In sample LC1724, a restricted viscous shear deformation is observed in the fine-grained
168 pseudotachylyte margin (Fig. 2a). However, this viscous creep was spatially highly restricted to a
169 zone < 1 mm wide adjacent to the margin, and has not deformed the fault walls of the anorthosite.

170 Samples N22 and LC1724 belong to two different networks of short (< 15 m long) type-2
171 pseudotachylyte-bearing faults developed in decametric pods of undeformed anorthosite bounded
172 by ductile shear zones (see Campbell et al. 2020). N22 was sampled from 68.054°N 13.361°E and
173 LC1724 from 68.056°N 13.377°E. Neither record unambiguous evidence for the sense of slip. The
174 anorthosite host rock in these samples consists of plagioclase (labradorite), clinopyroxene (diopside)
175 and orthopyroxene (enstatite), with minor amounts of olivine, hornblende, biotite, pleonaste spinel,
176 and garnet (Fig. 2). Olivine is mostly altered to iron oxides and enstatite, and is locally rimmed by
177 coronas of intergrown enstatite, pleonaste spinel, hornblende and biotite. Garnet may rim
178 orthopyroxene in contact with plagioclase.

179 The microcrystalline matrix of the LC1724 pseudotachylyte is primarily composed of plagioclase
180 (labradorite), orthopyroxene (enstatite) and clinopyroxene (diopside). Locally the pseudotachylyte
181 matrix may also contain biotite, potassium feldspar and hornblende. The pseudotachylyte vein
182 displays radiating microlites of plagioclase in the centre of the vein, becoming finer and more
183 granular towards the margin (Figs. 1e, 2a). Survivor clasts observed in this sample are composed
184 predominantly of plagioclase and orthopyroxene. The margin with the host rock is planar and has no
185 significant injection features visible within the thin section. The pseudotachylyte vein is 11 mm thick.

186 The microcrystalline matrix of the N22 pseudotachylyte is composed of plagioclase (andesine),
187 orthopyroxene (enstatite), clinopyroxene (diopside), hornblende and minor biotite (see Menegon et
188 al. (2017) for XRF analysis of sample N22). Survivor clasts are typically of plagioclase, orthopyroxene,
189 clinopyroxene and some apatite. A damage zone containing fragmented wall rock surrounded by
190 thin veins of pseudotachylyte extends for around 2 mm preferentially on one side of the main vein
191 (Figs. 2c,d). An additional sample of the N22 vein displays a large, cm-scale fragmented lithic clast
192 with an internal network of thin pseudotachylyte veins connected to the main vein (Fig. 2e). The
193 main pseudotachylyte vein has a maximum thickness of 18 mm.

194 4.2 Microstructure of clinopyroxene

195 4.2.1. Host rock

196 Across the undeformed host rock, clinopyroxene grains display orthopyroxene lamellae. In the
197 anorthosite internal blocks between shear zones (Fig. 1a), clinopyroxene only rarely has twins
198 evident (Fig. 3a) but twinning becomes present close to pseudotachylyte veins (Fig. 3b) at distances
199 of < 2cm (i.e. within a thin section).

200 EBSD maps of an elongate clinopyroxene grain (Fig. 2d, 'host CPX 1') lying 1-2 mm away from the
201 N22 pseudotachylyte fault vein margin indicate laminar and slightly discontinuous twinning on (001)
202 and to some extent on (100) planes (Figs. 3c-e). (001) twins are cut by a probable fracture,
203 represented as a low-angle boundary (LAB) in Fig. 3c. Lamellae of orthopyroxene also lie along (100)
204 planes of clinopyroxene. The grain orientation spread (GOS) of the clinopyroxene grain is < 5°, and is
205 lowest within the twins (Fig. 3d). Clinopyroxene in the immediate margin to the fault (Fig. 2d, 'host
206 CPX 2'), and cut by the pseudotachylyte vein, shows laminar (001) twinning (Fig. 3f-h). The GOS of
207 the clinopyroxene grain here is variable but always < 4° and again is lowest in the twin lamellae (Fig.
208 3g). Although the IPF (Z) map is fairly uniform, grain reference orientation deviation (GROD) maps
209 pick out subtle undulations parallel to (001) (Supp. Fig. 1a).

210 4.2.2 Clasts in pseudotachylytes

211 All survivor clasts of clinopyroxene display twinning on (100) and orthopyroxene lamellae along
212 (100) (Figs. 4,5). Clast 1 (Fig. 2d, 'clinopyroxene clast 1') is the most obviously elongate in shape (Fig.
213 4), measuring approximately 1000 x 300 µm, but all other clasts appear slightly elongate parallel to
214 the vein margin except for clast 3, where the clinopyroxene forms part of a lithic clast alongside
215 plagioclase (Fig. 2d, 'CPX clast 3'). (100) is typically parallel or sub-parallel to the vein margin in clasts
216 1 and 3-4. Clast 1, and to some extent clast 4 (Fig. 2f 'CPX clast 4'), are bent, visible in the curvature
217 of orthopyroxene lamellae (Fig. 4, 5c).

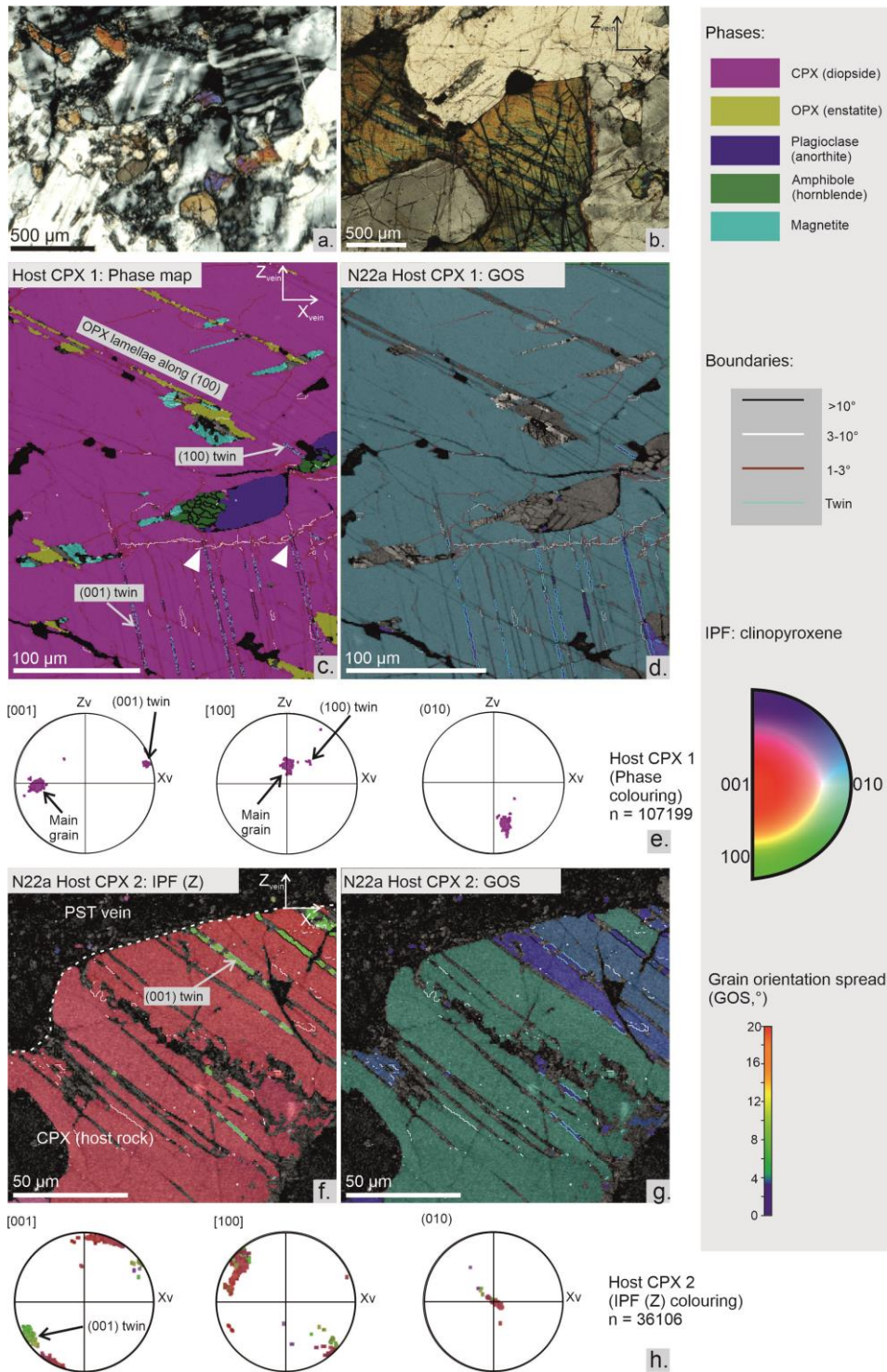


Figure 3. Microstructures of clinopyroxene in the host anorthosite; **a)** fine-grained clinopyroxene in anorthosite sampled within a shear-zone bounded block but away from any faults – shows detail of Fig. 1c (cross-polarised light); **b)** clinopyroxene situated 5 mm from vein edge (position indicated in Fig. 2d) showing twinning (cross-polarised image); **c)** EBSD phase map of clinopyroxene situated 2 mm from vein edge (position indicated in Fig. 2d, ‘Host CPX 1’) showing orthopyroxene lamellae, twin boundaries, and scarce low angle boundaries which truncate twinning (white arrowheads); **d)** grain orientation spread (GOS) map across same host rock clinopyroxene with values $< 5^\circ$, indicating low internal strain; **e)** pole figures for host clinopyroxene 1 as shown in c) with phase colouring **f)** IPF (Z) map of clinopyroxene in the immediate margin of the pseudotachylyte (position indicated on Fig. 2d, ‘Host clinopyroxene 2’) showing little change in orientation across the grain; **g)** GOS map of same clinopyroxene grain showing very little internal strain; **h)** pole figures for host clinopyroxene 2 as shown in f) with IPF(Z.)

218 Clasts 1 and 4, plus regions near the edges of clasts 2 and 3 (Figs. 2a, b) show moderately high GOS

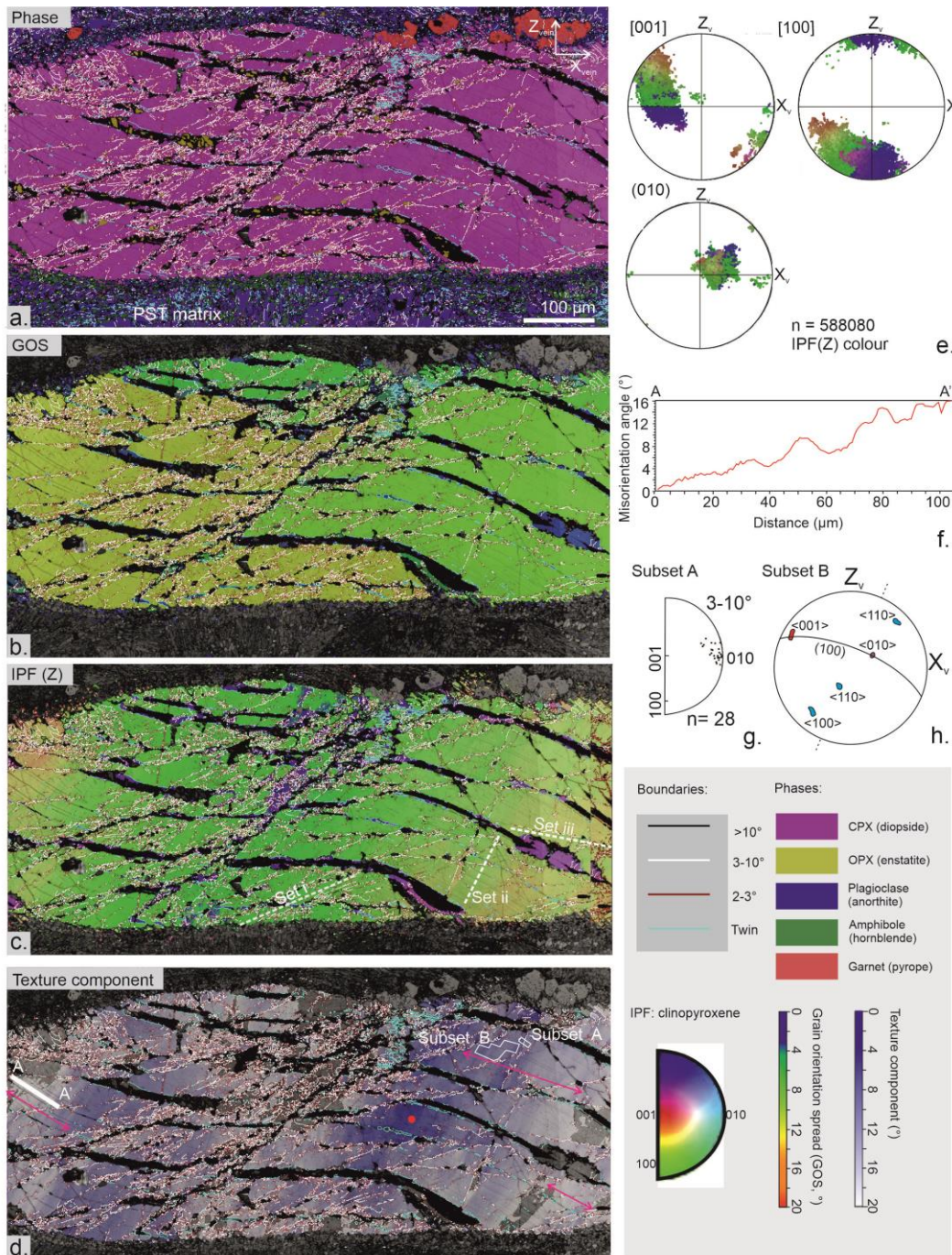


Figure 4. Microstructure of clinopyroxene clast '1' from EBSD analysis (position shown in Fig. 2d); **a)** Phase map highlighting bent orthopyroxene lamellae, twin boundaries and low angle boundaries; **b)** GOS map illustrating variable, but moderate, internal strain across the clinopyroxene grain. Twin lamellae have very low (blue) values; **c)** IPF (Z) orientation map of clinopyroxene. Lattice distortion of the entire grain is clear, as are twinned regions. Sets of low angle boundary orientations are labelled; **d)** texture component map (for clinopyroxene only) showing degrees of misorientation away from the reference point (red circle). Smaller-wavelength undulations are most easily seen here, strongly developed over regions indicated by pink arrows; **e)** pole figures (lower hemisphere) for [001] and [100] axes and poles to (010) planes of clast 1; **f)** misorientation profile from A-A' (location indicated in d.) showing regular 20-40 μm undulation of the lattice. The progressive increase in misorientation from point A is due to the long wavelength kinking of the clast; **g)** Rotation axes shown in crystal co-ordinates and crystal axes shown in sample co-ordinates for subset A, indicated in d.); **h)** pole figures for undulating region 'subset B' (indicated in d.), used for boundary trace analysis. The rotation axis [010] is indicated in purple and the suggested slip direction in red. The boundary trace parallel to the periodic undulation is indicated by the dashed lines.

219 up to 12° (Fig. 4b, 5d-e). Lower GOS values are seen within twins and within orthopyroxene

220 lamellae, and the lowest values occur where the orthopyroxene lamellae have recrystallized into a
221 polycrystalline aggregate. Clasts 1, 3, and 4 show systematic undulations with amplitudes of low
222 misorientation ($< 4^\circ$) with wavelengths typically of 20-40 μm , which are most evident on texture
223 component maps in regions free from twinning and low angle boundaries (Figs. 4d, 5f). These
224 features continue into the orthopyroxene lamellae. The change in orientation across these
225 undulations is continuous (Figs 4f, 5g) and we use the term 'periodic undulations' to refer to these.
226 The boundary trace analysis in clast 1 indicates that the undulations, as well as low-angle boundaries
227 parallel to them, are the result of slip on the [001](100) system with [010] as rotation axis (Fig. 4g,h).
228 However, the undulations in clast 4 do not give a clear rotation axis for boundary trace analysis,
229 though there is some clustering around [001] (Fig. 5h).

230 Low-angle boundaries are developed in different orientations, most clearly seen in clast 1 which has
231 three recognisable sets ('i-iii': Fig. 4c). Set (i) LABs cut and offset the orthopyroxene lamellae and the
232 periodic undulations. Clast 4 also has prominent linear LABs with some common orientations (Fig.
233 5c). As in clast 1, some linear LABs cut the undulations and offset sharply the orthopyroxene
234 lamellae (Fig. 5f).

235 Fine-grained clinopyroxene occurs in intracrystalline bands across some clasts. In clast 2, fine-
236 grained clinopyroxene has D_{equ} of 1.8-8.2 μm (Fig. 5a), and shows similar but dispersed orientations
237 relative to the parent clast (Supp. Fig. 2a-b). Rotation axes of these smaller grains are scattered and
238 do not clearly cluster around crystallographic rotation axes. The intracrystalline bands may also
239 contain hornblende (Fig. 5a), they crosscut some LABs (Fig. 5a), and they generally offset
240 orthopyroxene lamellae sharply. Clast 3 contains a similar example of a prominent intracrystalline
241 band with a width up to 15 μm (Fig. 5b). Fine-grained clinopyroxene in this band has a dispersed CPO
242 relative to the rest of the clast (Supp. Fig. 2c-d). Orthopyroxene lamellae, clinopyroxene twin
243 boundaries and any LABs are truncated and offset across the band. The band contains fine-grained
244 clinopyroxene alongside garnet and hornblende (Fig. 5). Both are also fine-grained (2-20 μm),
245 although the garnet coarsens at the edge of the mapped region, on the rim of the clinopyroxene
246 grain. This assemblage shows no sign of retrograde metamorphic reactions. Similar bands in
247 clinopyroxene filled with fine-grained clinopyroxene and amphibole were described from the
248 proximal damage zone of Nufjurd type-2 pseudotachylytes in Jamtveit et al. (2019), and were
249 interpreted as intracrystalline fractures that localized mineral reactions and phase nucleation.

250 [4.3 Microstructure of orthopyroxene](#)

251 [4.3.1 Host rock](#)

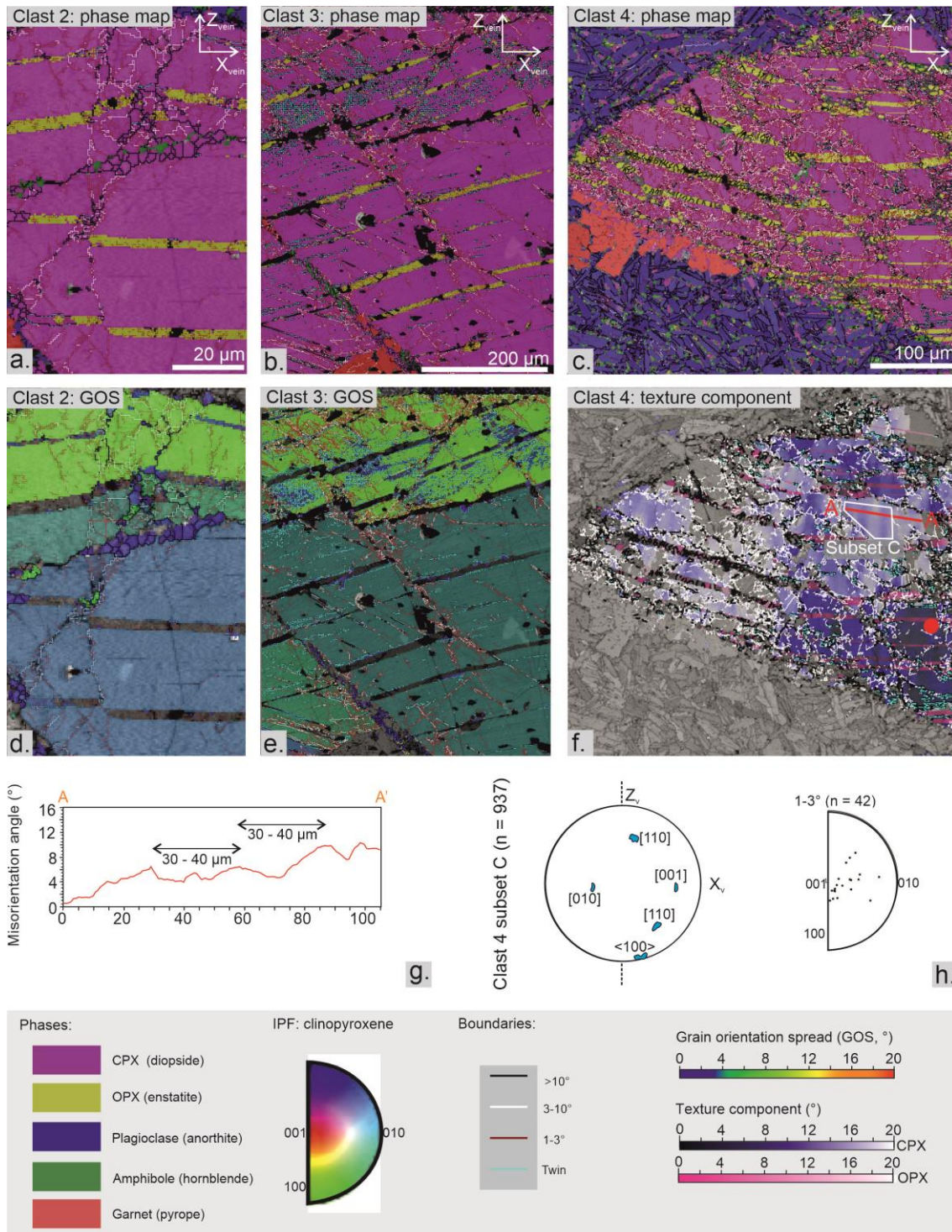


Figure 5. Microstructures of clinopyroxene clasts 2-4 from EBSD analysis (positions shown in Figs. 2d, f); **a)** phase map of part of clast 2; **b)** phase map of part of clast 3; **c)** phase map of part of clast 4; plus the surrounding pseudotachylyte matrix; **d)** GOS map of clast 2 (clinopyroxene only) showing increasing values towards the clast edge (top), and very low values in the fine grained crack fill; **e)** GOS map of clast 3 (clinopyroxene only) showing increasing values towards the clast edge, and very low values in clinopyroxene twins and in fine grained crack fill; **f)** texture component map for clast 4 showing misorientation relative to the reference point (red dot). Clinopyroxene is mapped in blue and orthopyroxene in pink; **g)** misorientation profiles for A-A' (shown in f.) highlighting regular undulations; **h)** orientation of axes in clinopyroxene clast 4 (location of subset c shown in f.). The boundary trace parallel to the periodic undulation is indicated by the dashed lines. Rotation axes are displayed in crystal co-ordinates for the same subset.

252 Orthopyroxene in the host rock away from the pseudotachylyte veins does not display

253 microstructural evidence of deformation, apart from weak to moderate undulose extinction. In the
254 host rock at the immediate margin of the pseudotachylyte veins N22 and LC1724, orthopyroxene
255 grains are cut by the faults (Figs. 2, 6, 7). These grains show a number of microstructures that are not
256 seen in more distal orthopyroxenes.

257 In N22, most of the orthopyroxene grain on the margin is fractured (Figs. 6a-b) but a transition is
258 seen from linear fractures (e.g. Fig. 6c) to a particularly fine-grained, pervasively fragmented regions
259 (Figs. 6 d-h). An orthopyroxene grain on the margin of the vein in LC1724 shows a similar feature
260 (Supp. Fig. 3). Within these fragmented regions, there is variation in grain size and shape between
261 subdomains of fine-grained, fairly equant fragments (root-mean-squared grain diameter of 1.4 μm
262 for N22, e.g. Fig. 6f), adjacent regions of coarser grains (Fig. 6e), and regions of larger, more angular
263 fragments locally dissected by intragranular fractures (Figs. 6d, g). The coarser regions (root-mean-
264 squared grain diameter of 2.6 μm for N22) have either equant or rather elongate morphology, with
265 some 120° triple junctions (Figs. 6e, 7b). Both the fine and the coarser (equant and elongate) grains
266 show abundant grain boundary porosity (Figs. 6a-c, 7b).

267 Elongate grains are seen in several fragmented orthopyroxene grains (Figs. 6e & h, 7, Supp Fig. 3)
268 lying adjacent to the vein margin and have their long axis at a high angle to the vein boundary.
269 Similar elongate fragments occur adjacent to large intragranular cracks within the orthopyroxene
270 host grain (Fig. 6h). Fragmented orthopyroxene occurs also adjacent to non-fractured clinopyroxene,
271 as shown in Supp. Fig. 3c, where orthopyroxene lamellae within clinopyroxene are fragmented next
272 to the vein margin (see Fig. 2 for location of this grain).

273 The GOS of the fine-grained fragmented orthopyroxene is low relative to the parent orthopyroxene
274 grain (Figs. 7a, Supp Fig. 3d). Low angle boundaries and higher GOS values are, however, seen in
275 some of the coarser fragments. The finer grains show dispersion of orientations away from the
276 crystallographic orientations of the parent orthopyroxene grain but otherwise are generally similar
277 to the parent orientation (Figs. 7b-d, Supp Fig. 3e-f). Misorientation axes are scattered in the
278 fractured grain region (Fig. 8e), although some clustering around [001] is present (Supp Fig. 3f). The
279 more elongate grains have a different CPO to the parent grain, they are preferentially elongate
280 parallel to [001], and show no obvious cluster of misorientation axes (Supp Fig. 3). In general, the
281 fragmented region shows a near- random distribution of misorientation angles between
282 uncorrelated grains but a higher frequency of misorientations $<35^\circ$ between neighbour grains than
283 for a random distribution (Fig. 7f, Supp. Fig. 3h).

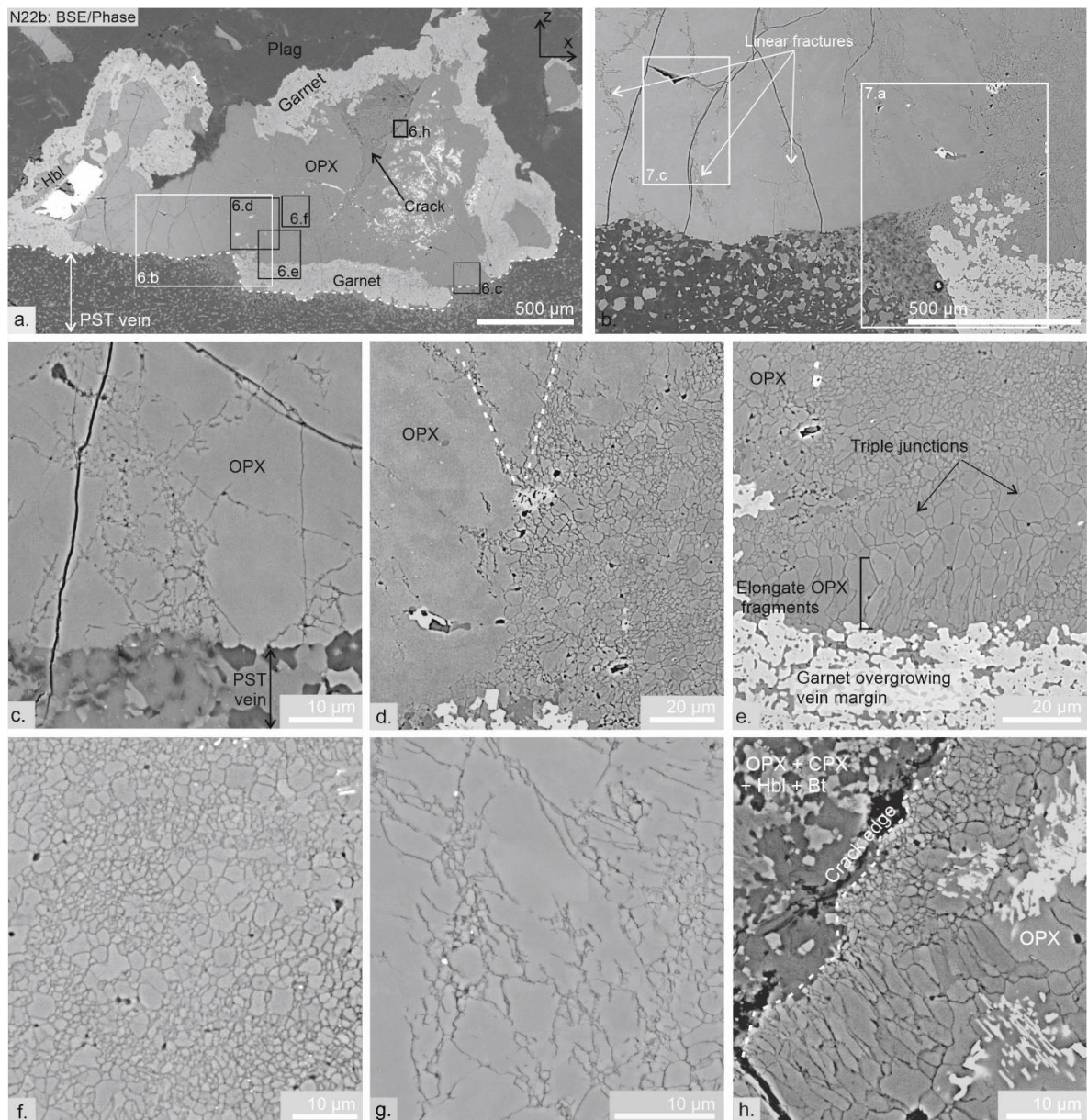


Figure 6. Backscattered electron (BSE) images of orthopyroxene grain and adjacent pseudotachylyte vein in sample N22: **a)** View of orthopyroxene grain on margin of pseudotachylyte vein with adjoining phases and subsequent image locations labelled; **b)** Higher magnification view of same grain illustrating fracture sets across left hand side of grain. Map locations for EBSD analysis shown in Fig. 7 are indicated; **c)** jigsaw-like fragmentation along cracks; **d)** edge of pervasively fragmented region. Dashed white lines indicate the main fracture orientations where they meet the fragmented region; **e)** Variation in fragment size and morphology in pervasively fragmented region; **f)** high-magnification image of pervasively fragmented region, showing finest grains; **g)** edge of fragmented region with coarse fragments; **h)** fragmentation of orthopyroxene around an internal crack filled with biotite plus minor orthopyroxene, clinopyroxene and hornblende.

284 The fractures evident in the BSE images of fragmented orthopyroxene (e.g. Figs. 6 b-c,g) correspond
 285 to LABs (i.e. with $< 10^\circ$ misorientation across them) or, less frequently, to high-angle boundaries on
 286 EBSD maps (Figs. 7a-c). Linear arrays of finer orthopyroxene plus minor clinopyroxene can be seen

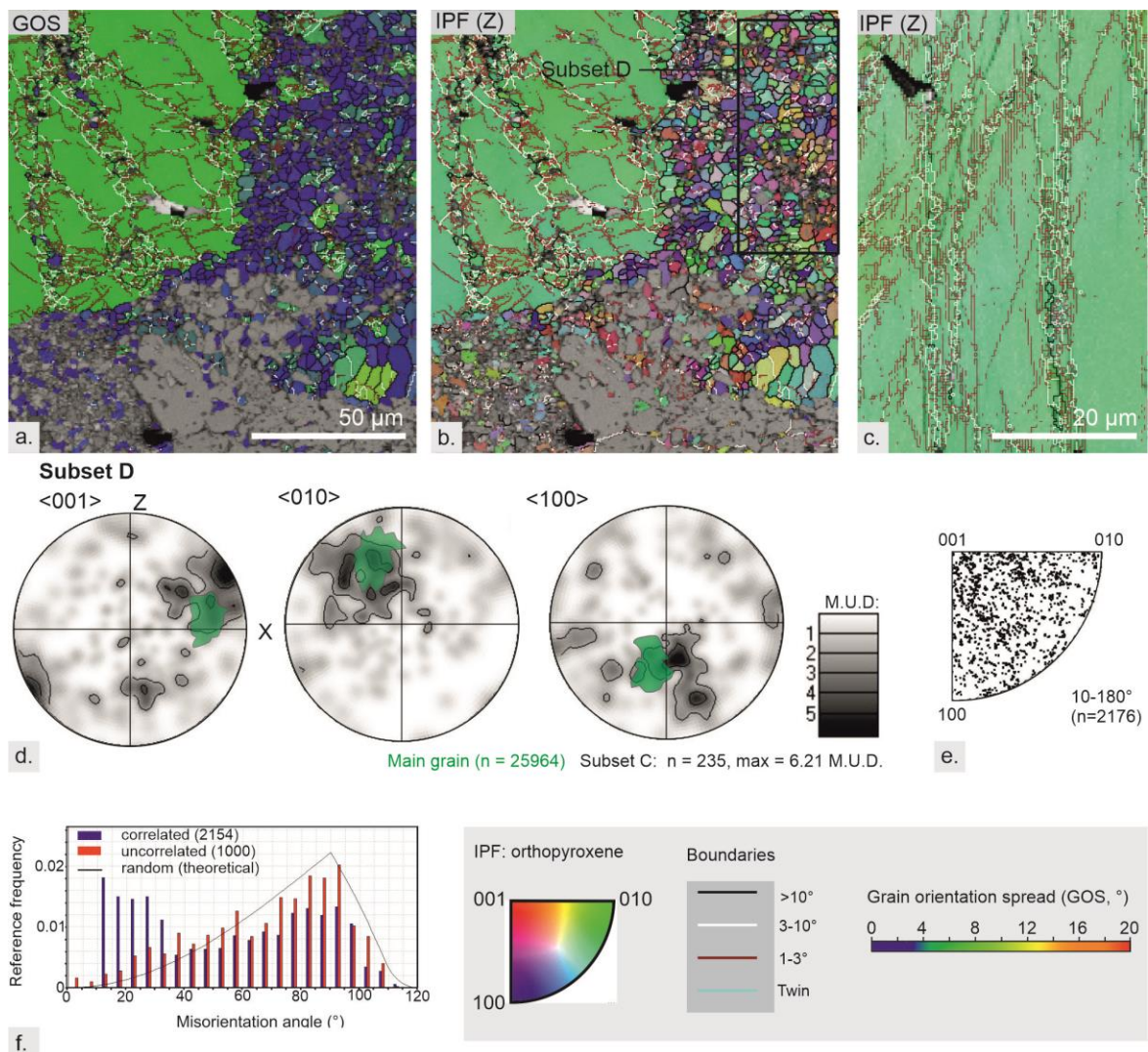


Figure 7. Microstructures of orthopyroxene in the host rock margin to a pseudotachylyte vein from EBSD analysis (map positions shown in Fig. 6): **a)** GOS map of edge of fragmented orthopyroxene **b)** IPF (Z) orientation map of orthopyroxene in same region as a); **c)** IPX (Z) orientation map of region in centre of orthopyroxene grain **d)** pole figures for sample of fragmented region – location of this subset D shown b); **e)** rotation axes (in crystal co-ordinates) pole figures for subset D; **f)** misorientation angle histogram for subset D.

287 along the larger of these cracks (Fig. 6b), with coalescence of the finer grained material in fracture
 288 intersections (Fig. 6c), but the orientation of the finer-grained orthopyroxene is nearly identical to
 289 that of the main grain (Figs. 7 b,c). These linear fractures appear truncated by the zones of more
 290 pervasive fracturing (Figs. 6d, 7a-b).

291 4.3.2 Grain size distribution in the fragmented domains

292 Some of the regions of fragmented orthopyroxene studied for grain size analysis are shown in Figs. 6
 293 d-g (sample N22) and Supp. Fig. 3a-b (sample LC1724). The sampled set consisted of 2033 grains
 294 from N22 and 421 from LC1724. All analysed images were taken from the fragmented regions of the
 295 orthopyroxene grains shown in Figs. 6a & 7a. The grain size distribution curve for both samples
 296 shows differences between the smaller and larger grain size ranges (Supp. Fig. 4). Both power law

297 and log normal lines of best fit were calculated for sections of the distributions. Using the power law
298 exponent, for N22, the slope of the finer grain size distribution was 2.3 and for the coarser range,
299 1.2. For LC1724, the finer grained range gave a slope of 1.6, and the coarser range, 3.1 (Supp. Fig. 4)
300 The break in slope is less pronounced in LC1724 but is nevertheless best fit by two separate power
301 law trendlines. In N22 the break of slope is clear and occurs around 4.7 μm .

302

303 4.3.3 Clasts in pseudotachylytes

304 Figure 8 shows the EBSD maps of an orthopyroxene clast in the pseudotachylyte matrix of sample
305 LC1724, consisting of microlitic plagioclase and granular clinopyroxene, hornblende and
306 orthopyroxene (Figs. 1e, 8a). The clast occurs at a distance of 3.4 mm from the margin of the PST
307 vein. Undulose extinction and deformation bands are visible optically (Fig. 1e). EBSD mapping
308 reveals that these bands represent intracrystalline arrays of fine-grained orthopyroxene with very
309 minor interstitial clinopyroxene and hornblende (Fig. 8a). The fine orthopyroxene grains have a
310 maximum GOS of 0.59 (Fig. 8b), a maximum D_{equ} of 6.3 μm and a root-mean squared D_{equ} of 2.1 μm .
311 These arrays dissect the host orthopyroxene clast into domains that have accumulated different
312 amounts of internal deformation, as evident from their different GOS values, overall in the 3-8°
313 range (Fig. 8b).

314 The orthopyroxene clast shows slight but repeated undulations with parallel orientation (Fig. 8c,
315 Supp. Fig. 1b). These undulations are locally parallel to sharp, linear low-angle boundaries (1-3°) (Fig.
316 8c). These periodic undulations and the 1-3° low-angle boundaries occur on a semi-regular
317 wavelength of 10-20 μm , giving a crenulated undulose effect (Fig. 8d). The misorientation axis
318 associated with these bands is [001] (Fig. 8e), which is consistent with slip on the (100) [010] system
319 assuming a tilt boundary geometry. The undulations and the low-angle boundaries are cut by the
320 arrays of fine-grained orthopyroxene.

321 The fine-grained orthopyroxene share a CPO with the host clast, although some dispersion is present
322 (Figs. 8f). The dispersion predominantly occurs around [001]. Polygonal networks of low-angle
323 boundaries, potentially indicating the development of subgrains, have not been observed in the
324 clast.

325 5. Discussion

326 5.1 Overprinting relationships between deformation microstructures

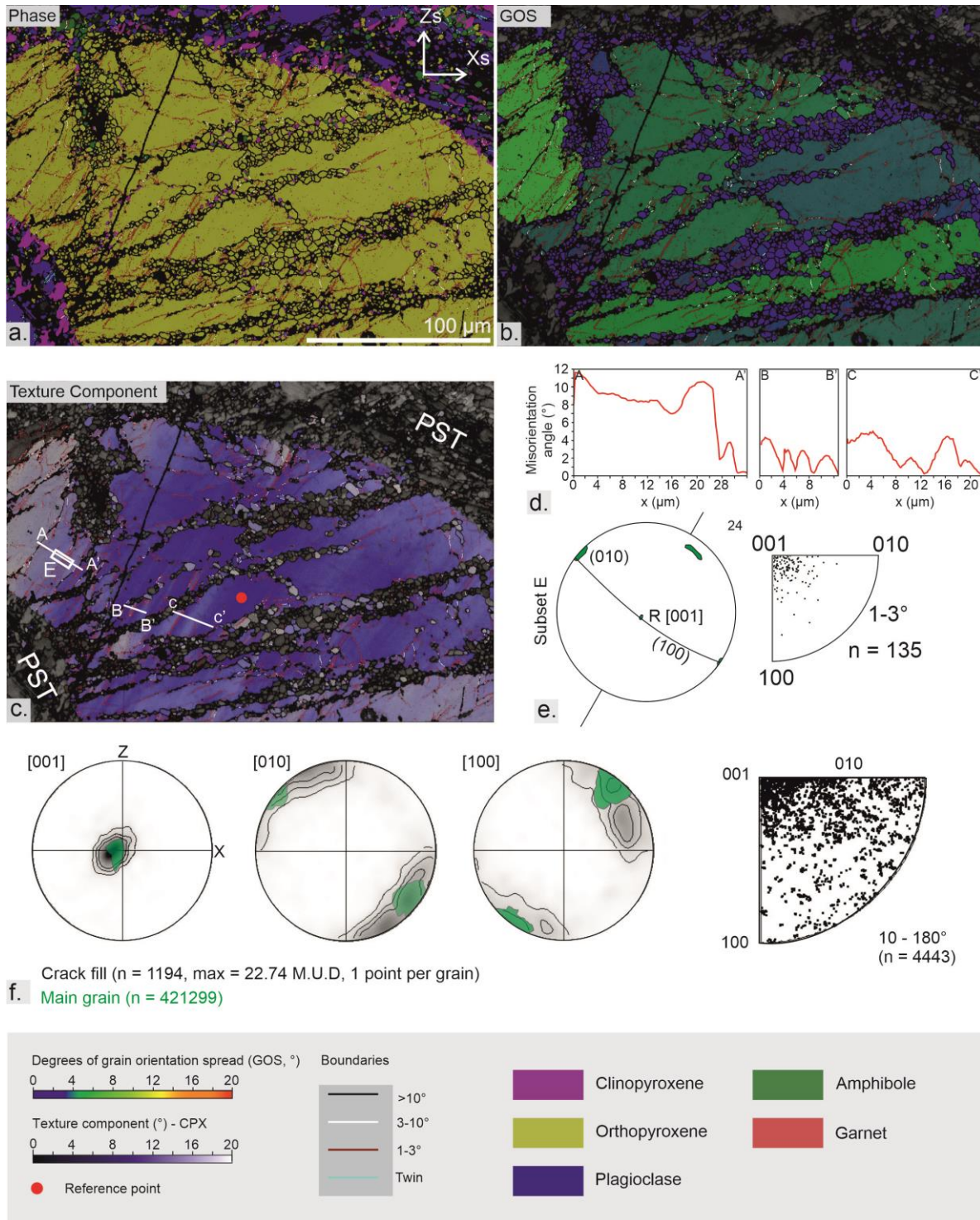


Figure 8. Microstructures of orthopyroxene clast from EBSD analysis; **a)** Phase map of analysed region of clast and surrounding pseudotachylyte matrix; **b)** GOS map of orthopyroxene. Fine-grained arrays of orthopyroxene have low GOS values (blue colouring); **c)** Texture component map of orthopyroxene, red dot locates reference point; **d)** misorientation profiles along A-A' B-B' and C-C', indicated in c); **e)** pole figure and low-angle rotation axes (in crystal coordinates) for subset D, location shown in c); **f)** pole figures and high-angle rotation axes for the fine-grained orthopyroxene arrays within the clast. Green overlay shows distribution of points from the main grain.

327 Deformation twins occurs pervasively in clinopyroxene, both in clasts in the pseudotachylyte veins as
 328 well as in host rock grains situated at least up to 8 mm away from the vein margin (Fig. 3b).

329 Deformation twinning predominantly developed on (001), although additional (100) twins are
330 developed in clast 3 (Fig. 5b) where the clustering of (100) twins near the clast boundary implies that
331 additional (100) twinning may have been driven by deformation conditions along the fault. However,
332 twin boundaries are generally bent and cut by LABs, by cracks, and by periodic low (1-3°)
333 misorientation bands (Figs. 4, 5), implying that twinning is typically the earliest microstructural
334 record of deformation in clinopyroxene, and extends some distance into the wall-rock.

335 Other deformation microstructures are limited to clasts within the pseudotachylyte fault zone,
336 suggesting that they relate to highly localised deformation associated with the seismic rupture.
337 These are the periodic undulations with 20-40 μm wavelength, which overprint orthopyroxene
338 exsolution lamellae (Fig. 5f) and deformation twins, but are cut and offset by linear LABs (Fig. 4). The
339 LABs are cut by the final stage of deformation in the clinopyroxene clasts, fracturing and grain
340 growth in intracrystalline bands of fine-grained clinopyroxene \pm amphibole \pm garnet (Fig. 5a,b).

341 In orthopyroxene, fracturing and fragmentation is preserved in grains in the wall rock margin as well
342 as in survivor clasts. In the wall-rock margin, the dominant microstructure is fracturing (Figs. 6b-c)
343 and local regions of pervasive fragmentation (Figs. 6-7, Supp. Fig. 3). In the orthopyroxene clast
344 analysed with EBSD, undulating misorientation resulting from glide on (100)[010] is cut by
345 intracrystalline bands of fine-grained orthopyroxene \pm clinopyroxene \pm amphibole (Fig. 8). Because
346 other orthopyroxene clasts show pervasive fragmentation similar to the margin grains (Supp. Fig.
347 3,5), we suggest that the analysed orthopyroxene clast in Fig. 8 preserves the earlier signature of
348 dislocation glide, which has escaped fragmentation.

349 In summary, we interpret these overprinting relationships to reflect the pre- to co-seismic
350 deformation of pyroxene in response to local stress amplifications that triggered the generation of
351 type-2 pseudotachylytes in Nufjord. In the following sections, we propose a conceptual model for
352 the association of these stress changes with the seismic cycle already partly recorded by the
353 presence of pseudotachylyte.

354

355 5.2 High stress loading: deformation by low-temperature plasticity

356

357 Twinning via (100)[001] in clinopyroxene occurs at a critically resolved shear stress of 100-140 MPa
358 but is not dependent on temperature or strain rate (Kollé & Blacic, 1982). The presence of twinning
359 in host rock clinopyroxene grains away from the vein margin suggests that this early stage of
360 deformation was driven by stresses that were not entirely localised to the fault plane. This may be

361 related to the earliest heterogeneous stress amplifications that built up prior to failure, less localised
362 to the eventual rupture zone than the later microstructures in clasts that all cross-cut twinning.

363 Most clinopyroxene clasts illustrated here show deformation by low-temperature plasticity
364 controlled by dislocation glide along (100)[001], producing LABs and undulating misorientation that
365 cut the twin boundaries and the orthopyroxene exsolution lamellae. (100)[001] is the typical glide
366 system in clinopyroxene (Avé Lallemant, 1978; Ingrin et al., 1992; Kirby & Kronenberg, 1984; Kollé &
367 Blacic, 1983; Raleigh & Talbot, 1967). In our samples, evidence of any transition to dislocation creep
368 is absent, consistent with the relatively low temperature conditions of deformation for crystal
369 plasticity in clinopyroxene (e.g. Bystricky & Mackwell 2001). Flow laws extrapolated to natural strain
370 rates for dislocation glide of diopside require several 100 MPa or GPa of differential stress for
371 Peierls-controlled glide to occur in clinopyroxene (Fig. 9). Results from the micro-indentation tests of
372 Dorner & Stöckhert (2004) suggest that, at relatively low strain rates of 10^{-14} s^{-1} and a temperature
373 range of 600-700°C, between 1.6-2.0 GPa would be needed to activate Peierls-controlled glide. If
374 strain rates were to increase towards seismic strain rates, for example a rapid strain rate of 10^{-3} s^{-1} ,
375 the required flow stress increases to 3.7-3.9 GPa (Fig. 9). Based on the flow law for Peierls-controlled
376 glide of Kollé & Blacic (1983), at temperatures of 600-700°C strain rates $> 10^{-12} \text{ s}^{-1}$ are necessary to
377 induce glide, and at strain rates of 10^{-9} s^{-1} or greater, critical resolved shear stresses would be > 1
378 GPa (at 700°C) and > 3 GPa (at 600°C) (Fig. 9). This glide law was observed by Kollé & Blacic (1983) to
379 initiate at critically resolved shear stresses > 520 MPa in hedenbergite crystals poorly orientated for
380 twinning; in crystals where twinning was possible, dislocation glide required temperatures > 850 °C
381 under their experimental conditions. Without knowing the stress orientation, it is not possible to
382 convert an equivalent differential stress, but the differential stress must be at least twice the
383 resolved shear stress. We therefore infer that the low-temperature plasticity microstructures
384 observed in clinopyroxene clasts occurred as a response to transient and localised differential
385 stresses in excess of 1 GPa. The localisation of these microstructures to the clasts, and not in the
386 clinopyroxene grains which now form the margin to the pseudotachylyte vein, suggests that these
387 high stresses were localised to the rock volume that subsequently formed the pseudotachylyte fault
388 vein. However, overprinting by fracturing indicates that this localisation occurred prior to passage of
389 the rupture tip.

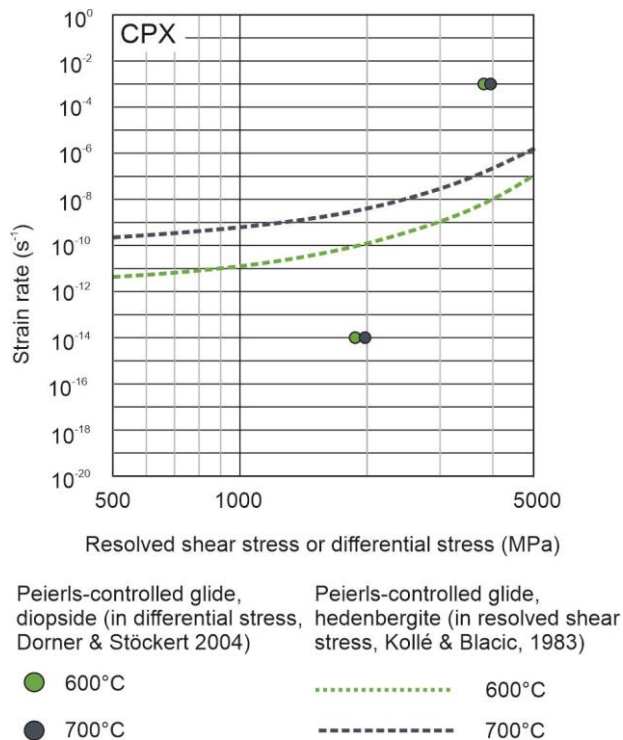


Figure 9. Two flow laws for Peierls-controlled glide in diopside (Dorner & Stöckert, 2004) and hedenbergite (Kollé & Blacic, 1983) at temperatures for deformation in Nusfjord (600-700°C). The law from Dorner & Stöckert (2004) is shown at strain rates of 10^{-14} s^{-1} (i.e. a background geological strain rate) and at a very rapid 10^{-3} s^{-1} (for approximation of acceleration towards seismic slip rates). The law from Kollé & Blacic (1983) is for Peierls glide on (100) [001] for $< 900^\circ\text{C}$ and $> 520 \text{ MPa}$. Note that the x-axis shows differential stress for Dorner & Stöckert (2004) but resolved shear stress for the laws of Kollé & Blacic (1983).

390 The regular 20-40 μm wavelength periodic undulation of the clinopyroxene lattice (Figs. 4f, 5g) bears
 391 some similarities to the short-wavelength undulatory extinction (SWUE) recognised in quartz
 392 (Trepmann & Stöckhert, 2013) and olivine (Druiventak *et al.*, 2012) ‘kick-and-cook’ experiments,
 393 although the undulation in clinopyroxene has a longer wavelength. The undulose misorientation is
 394 characterised purely by continuous sinusoidal curvature of the crystal lattice, which was
 395 accommodated by glide along the (100)[001]. Similar periodic undulations occur also in
 396 orthopyroxene clasts (Fig. 8d) and are consistent with dislocation glide on (100)[010] (Fig. 8e).

397 The formation of SWUE in quartz was attributed to high stress dislocation glide (‘kick’-phase) that
 398 generates lamellae of tangled dislocations (Trepmann & Stöckhert, 2013). Natural comparisons to
 399 SWUEs have been proposed in quartz (Brückner & Trepmann, 2021, Birtel & Stöckhert, 2008,

400 Trepmann & Seybold, 2019) and olivine (Matysiak & Trepmann, 2012) but not, to our knowledge,
401 previously in pyroxenes. The generation model for SWUEs of Trepmann & Stöckhert (2013), invoking
402 dislocation glide under high stresses caused by seismic loading, is inviting because of the shared
403 deformation mechanism (glide) observed in these pyroxenes, and because of the seismic context of
404 the Nufjord samples. The parallels are especially clear in the recent work of Brückner & Trepmann,
405 (2021) who observe SWUEs in quartz adjacent to pseudotachylytes. We propose that the periodic
406 undulations in clinopyroxene were produced by a low-temperature plasticity response to the highest
407 stresses localised around the eventual fault plane. After twinning, the periodic undulations are the
408 next earliest microstructure to form in clinopyroxene, and in orthopyroxene are cut by fractures.
409 Hence they are potentially related to the stress concentrations during loading, preceding eventual
410 rupture.

411 SWUEs in quartz and olivine were attributed to high-stress loading of the mid- to lower-crust via
412 shallower earthquake activity (Birtel & Stöckhert, 2008; Malysiak & Trepmann, 2012; Trepmann &
413 Stöckhert 2013). The context of the seismic environment in Nufjord, where type-2
414 pseudotachylytes represent the in-situ nucleation of short earthquake ruptures (Campbell et al.
415 2020), fits better with the observations of Brückner and Trepmann (2021) that such glide-controlled
416 microstructures also occur adjacent to in situ seismic rupture within the mid- to lower- crust. Our
417 evidence supports transient high stress loading either being a result of local stress amplifications
418 preceding and eventually causing rupture nucleation (Campbell et al., 2020), or as a response to high
419 rupture tip stresses (Reches & Dewers, 2005). The former is preferred due to the overprinting of glide
420 structures in orthopyroxene by later fragmentation that can be linked with more confidence to
421 dynamic rupture tip processes.

422

423 5.3 Coseismic deformation: pulverisation of orthopyroxene

424

425 The fine-grained orthopyroxene at the pseudotachylyte fault vein margin (Figs. 6-8) is interpreted to
426 have formed via brittle grain size reduction, based on: a) the fracture systems evident in BSE
427 micrographs (Fig. 6) and the jigsaw-breccia type grain shapes preserved in some fine-grained regions
428 (Fig. 6g), and b) the absence of polygonal subgrains from the interior of the large orthopyroxene
429 fragments, in accordance with the expected lack of recovery in orthopyroxene at the deformation
430 temperature of 700-750 °C (e.g. Kohlstedt & Vander Sande, 1973; Kanagawa et al., 2008). The lack of
431 shear between large fragments (Figs. 6,7) supports that pulverisation, rather than cataclasis, was the
432 main fragmentation process in orthopyroxene. The lack of shear is also evident in the overlap in
433 crystallographic orientation between the fine grains and the coarser fragments (Fig. 7d, see also

434 Petley-Ragan et al., 2019 and Soda & Okudaira, 2018). An alternative explanation of thermal shock
435 was ruled out due to the lack of fracturing in the orthopyroxene clast (Fig. 8), which, being within the
436 vein, should have experienced higher coseismic temperatures than the wall rock (Papa et al., 2018),
437 although other orthopyroxene clasts do show pervasive fragmentation (Supp. Fig. 5).

438 Although pulverisation is considered to be depth-limited by increasing confining pressure (Aben et
439 al., 2017; Yuan et al., 2011), pervasive damage zones extending up to 200 m from the fault have
440 been exhumed from crustal depths below the frictional viscous transition (Sullivan & Peterman,
441 2017). Interpretations of pulverisation of single grains have recently accumulated from
442 microstructural studies of lower crustal seismicity in both naturally and experimentally deformed
443 rocks (Austrheim et al., 2017; Soda and Okudaira, 2018; Incel *et al.*, 2019; Petley-Ragan *et al.*, 2019;
444 Song *et al.*, 2020). Minerals observed to undergo pulverisation-style fragmentation include
445 plagioclase (Soda & Okudaira, 2018), garnet (Austrheim et al., 2017; Incel et al., 2019; Petley-Ragan
446 et al., 2019; Song et al., 2020) and diopside (Petley-Ragan et al., 2019). In the Nusfjord samples,
447 orthopyroxene is the only mineral to show microstructures compatible with pulverisation-style
448 fragmentation.

449 Pulverisation-style fragmentation, particularly where tensile fracturing is involved, is attributed to
450 dynamic rupture tip stress fields that overcome the high confining pressure (Reches & Dewers,
451 2005), but has also been linked to the passage of seismic shockwaves ahead of the rupture front
452 (Doan & Gary, 2009) and by impulsive coseismic loading and unloading of the wall-rocks (Brune,
453 2001). The asymmetry of fragmentation observed in the field along major tectonic faults favours a
454 link with the asymmetric rupture tip stress fields, where one side of the tip is in compression and the
455 other in tension (Dor et al., 2006; Petley-Ragan et al., 2019; Reches & Dewers, 2005; Wilson et al.,
456 2005; Xu & Ben-Zion, 2017). Although supershear ruptures may favour pulverisation (Yuan et al.,
457 2011), sub-shear ruptures should also induce extreme stress and strain rate conditions a few mm
458 from the rupture – one calculation predicts 5 GPa tensional stress and $\sim 10^5 \text{ s}^{-1}$ dilation in this zone
459 (Wilson et al., 2005). In our samples, it is not easy to judge whether the pulverisation occurs on one
460 side of the fault only, because there is no orthopyroxene visible in the opposing wall to compare
461 with. Whilst fragmented orthopyroxene occurs within clasts in the vein, the delocalisation effect of
462 the pseudotachylite melt makes it impossible to know where the initial rupture plane was in relation
463 to the in situ position of that grain. There is evidence for injection veins and damage on both sides of
464 the fault in one sample (Fig 2c-d), which may dispute asymmetry (although injection veins are not
465 always linked to rupture-tip stress fields) – however, the alternative models of impulsive loading

466 cycles or shockwaves (Brune, 2001, Doan & Gary, 2009) are also coseismic processes and do not
467 change our interpretation of the timing of these microstructures.

468

469 5.4 Grain growth of orthopyroxene driven by short-term heat pulse

470

471 Many of the orthopyroxene fragmented grains are somewhat modified in shape. Grain growth from
472 the fine-grained fragments is apparent in the elongate orthopyroxene grains, as well as in regions
473 with well-developed 120° triple junctions (Fig. 6e). Grain-size distributions (Supp. Fig. 4) are
474 commonly used to determine processes of fracturing, faulting, and grain growth (e.g. Sammis *et al.*
475 1986), although the various mechanisms of brittle fragmentation are not always easily
476 distinguishable via this analysis (Stünitz *et al.*, 2010; Wilson *et al.*, 2005). The observed range of 2D
477 slope values in our analysis, 1.2-3.1 (Supp. Fig. 4), is comparable with grain size distributions
478 reported for mid- to lower-crustal seismic deformation (Aupart *et al.*, 2018 and references therein;
479 Jamtveit *et al.*, 2019; Soda and Okudiara, 2018; Song *et al.*, 2020) including those attributed to
480 coseismic pulverisation of garnet, olivine and plagioclase. Neither of our samples are conducive to a
481 single best-fit power law or log normal distribution, with the break in slope estimated at a diameter

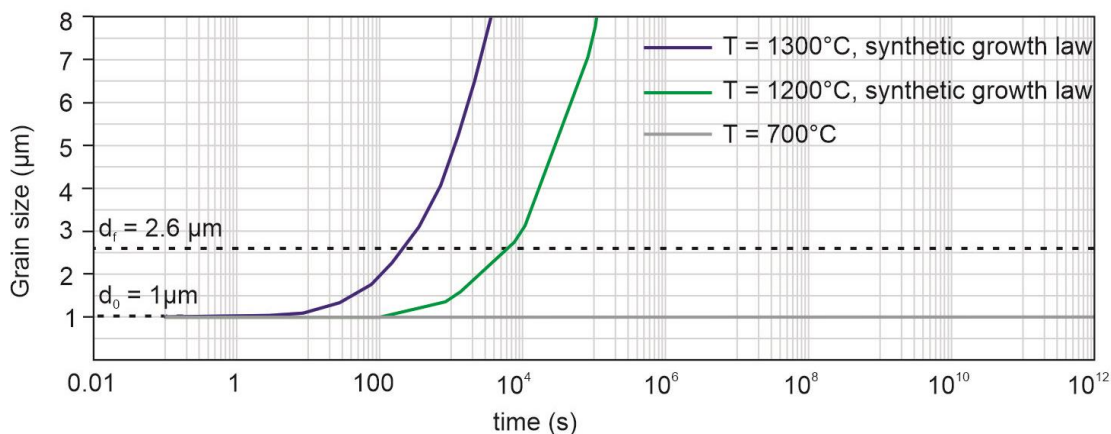


Figure 10. OPX grain growth modelling from initial diameter of 1 µm. Growth law parameters from the synthetic samples of Skemer & Karato (2007) are used to compare rates for 1300 °C and 1200 °C; for 700 °C, the rate constant k (rate constant) is extrapolated from enthalpy and k_0 values provided in the same publication

482 of around 4.7 µm for both samples. We suggest that this change in slope reflects modification of the
483 original fragmentation grain size by the subsequent grain growth apparent in the BSE images. This is
484 consistent with the findings of Keulen *et al.* (2007) and Aupart *et al.*, (2018) that changes in GSD
485 slope reflect a switch in grain processes.

486 The CPO of the elongate grains differs to that of the more equant fragments, which tend to be
487 similar to the parent CPO (Supp. Fig. 3f-g). The short axes of the elongate grains are of a similar size
488 to the diameter of the equant grains, suggesting that the elongate grains may have formed via a mix
489 of rotation and growth of existing fragments. The shape preferred orientation is always at a high
490 angle to the vein edge (Figs 6-7, Supp. Fig. 3) and the grain elongation is predominantly parallel to
491 [001], which has been reported as the fastest diffusion and growth direction in orthopyroxene
492 (Milke et al., 2013; Dohmen et al., 2016). This elongation is also observed at the edge of a large
493 intracrystalline tensile crack within a host rock margin orthopyroxene grain (Figs. 6a,h) which
494 extends between points of 0.34 - 1.09 mm perpendicular distance from the pseudotachylyte vein
495 edge. The apparent orientation of the crack forms a high angle to the fault vein, suggesting that the
496 crack was tensile, as does the parallel elongation of the orthopyroxene, perpendicular to the crack.
497 This geometry is similar to tensile cracks formed within dynamic stress fields linked to crack tip
498 propagation (Ngo et al., 2012), suggesting that it may have formed concurrent with the
499 pulverisation-style fragmentation within the grain. The distribution of the elongate grains along the
500 edge of this crack as well as along the pseudotachylyte vein margin therefore implies that elongate
501 grain growth occurred after fragmentation but potentially concurrent with continued slip and the
502 associated frictionally generated thermal pulse that drove melting along the fault plane.

503 Because of the transience of frictional heating, grain growth needs to take place during, or
504 immediately after, seismic slip. Using the orthopyroxene grain growth laws of Skemer & Karato
505 (2007), we assess the potential growth time necessary for a starting orthopyroxene fragment size of
506 1.0 μm at temperatures ranging from 1300 $^{\circ}\text{C}$ - close to typical pseudotachylyte maximum melt
507 temperatures (Sibson & Toy, 2006) - down to an ambient temperature of 700 $^{\circ}\text{C}$ (Fig 10.). At 700 $^{\circ}\text{C}$,
508 the orthopyroxene will not achieve the required grain size of $D_{\text{equ}} = 2.6 \mu\text{m}$ (for the elongate grains)
509 within 3 Ga, implying that some form of heat pulse must be required for grain growth. At
510 temperatures around 1300 $^{\circ}\text{C}$ the required grain growth may be achieved within 16 minutes and at
511 1200 $^{\circ}\text{C}$, within 3 hours (Fig. 10). These temperatures can be feasibly generated during coseismic
512 frictional heating, so that growth of the elongate grains may have initiated during slip.

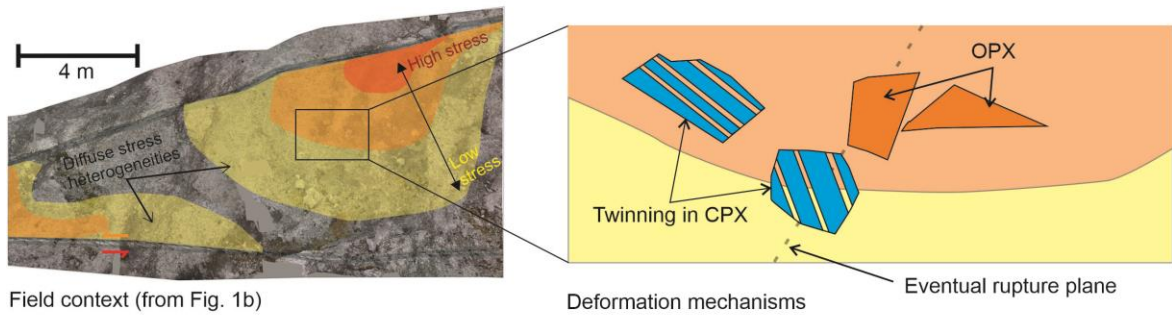
513

514 [5.5 Conceptual model of pre-and co-seismic deformation in pyroxenes](#)

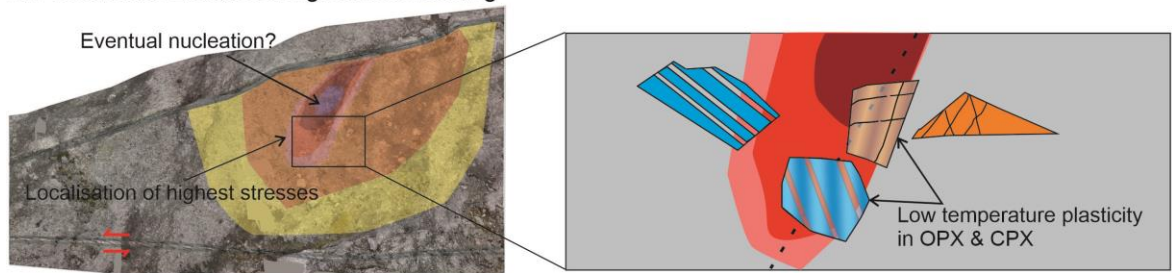
515 Based on the overprinting relationships of microstructures in the pyroxenes (sections 4.2-4.3) and
516 our interpretations of their deformation mechanisms plus resulting stress and temperature
517 implications, we suggest a conceptual model of pre- and co-seismic deformation of clino- and
518 orthopyroxene (Fig. 12).

519 1. Distributed twinning seen in clinopyroxene appears to be spatially associated with
 520 pseudotachylyte veins but are not as localised as subsequent deformation microstructures.
 521 The critical shear stresses associated with clinopyroxene twinning (Kollé & Blacic, 1982) are
 522 not especially high relative to expected failure strength; twinning may relate to progressive
 523 stress amplification prior to the failure stress being reached (Campbell et al., 2020).

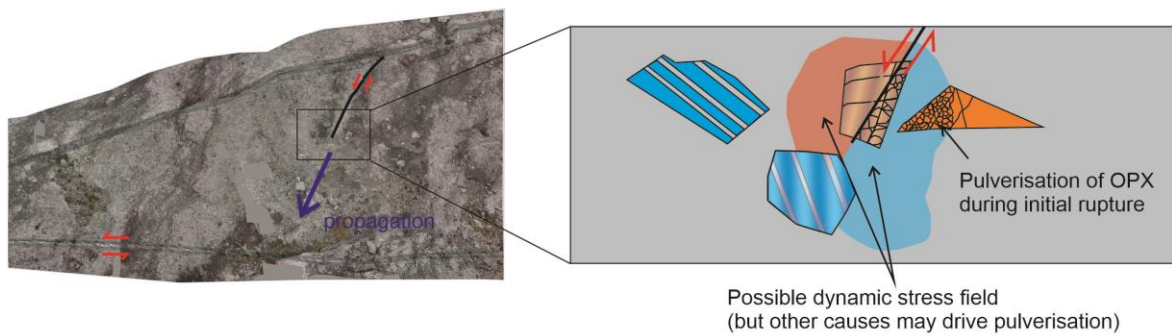
1. Preseismic: Initial stress loading



2. Preseismic: Localised high stress loading



3. Coseismic: pulverisation of orthopyroxene



4. Coseismic: thermal heat pulse

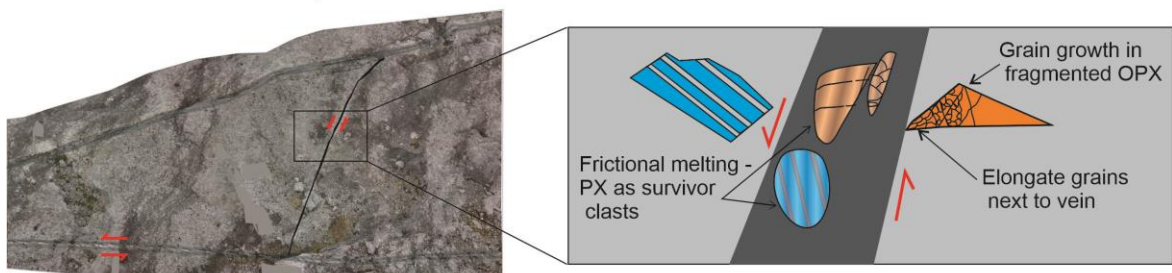


Figure 11. Proposed order and association of pyroxene microstructure with potential rupture processes. A conceptual example from the context of the shear-zone bounded block shown in Fig. 1b – in this example, the pre-seismic stress loading is thought to be driven by the activity of the shear zones (Campbell et al., 2020).

- 524 2. Low temperature plasticity in clinopyroxene and orthopyroxene is predominantly found
525 within clasts, suggesting much more pronounced localisation of stress (potentially > 1 GPa,
526 Fig. 12) around the eventual rupture plane. This is consistent with interpretations made for
527 similar high-stress dislocation glide-controlled microstructures observed in both naturally
528 and experimentally deformed rocks (Druiventak *et al.* 2011; Matysiak & Trepmann 2012;
529 Trepmann *et al.* 2013).
- 530 3. Low temperature plasticity is overprinted by pulverisation-style fragmentation in
531 orthopyroxene, which most likely relates to dynamic stress fields related to the passage of
532 the rupture tip (the ‘fault tip process zone’ of Petley-Ragan *et al.*, 2018 – their Fig. 4), or
533 alternatively may relate to impulsive loading or shockwaves. There appears to be no
534 microstructural record for this stage in the clinopyroxene.
- 535 4. After the passage of the rupture tip, frictional heating during continued seismic slip melts
536 phases along the fault plane, eventually cooling to form the pseudotachylyte vein.
537 Fragments of pyroxene and plagioclase, sourced from the fault walls and comminuted
538 material, may survive, unmelted, as clasts. Conduction of the frictional heat pulse into the
539 wall rock is a feasible driver of (oriented) grain growth within the fragmented orthopyroxene
540 immediately adjacent to the pseudotachylyte vein.

541

542 5. Conclusions

543

544 Deformation mechanisms in both clino- and orthopyroxenes spatially associated with ancient
545 seismogenic faults from Nusfjord (Lofoten, Norway) record increasing localisation of progressively
546 higher stress (up to GPa in magnitude) prior to rupture, preceding pulverisation-style fragmentation
547 of orthopyroxene potentially linked to the passage of the rupture tip. The spatial association of these
548 microstructures with a single-slip pseudotachylyte-bearing fault plane, constrained to represent
549 seismic rupture nucleating at lower crustal depths of 25-30 km, implies that the sequence of
550 overprinting microstructures may be linked to increasing loading and eventual rupture during one
551 lower crustal seismic cycle.

552 The extent to which low-temperature plasticity within lower crustal granulites can accommodate
553 transient stress amplifications may be an important control on when and where rupture and
554 subsequent seismic damage can initiate with the lower crust. Intracrystalline deformation of phases

555 along the fault plane and in the damage zone is an increasingly recognised and valuable record of
556 the short-term changes to the stress regime prior to rupture in lower crustal rocks.

557

558 Acknowledgements

559 This work was supported by the UK Natural Environment Research Council (grant NE/P001548/1
560 “The Geological Record of the Earthquake Cycle in the Lower Crust”). We thank colleagues at the
561 Plymouth Electron Microscopy Centre for guidance and support with SEM analysis. Sample N22 was
562 collected by Elliot Wood and Katherine Harris during their MGeol project at the University of
563 Plymouth. Unfortunately Elliot is no longer with us to see the completion of this work. This paper is
564 dedicated to him, and to his passion for science and nature.

565 Open Research

566 Available data in support of this work include: unfiltered EBSD datasets, images used for grains size
567 data analysis, spreadsheets showing calculations for grain size data analysis and grain growth
568 modelling. These data are available at the British Geological National Geoscience Data Centre via
569 <https://webapps.bgs.ac.uk/services/ngdc/accessions/index.html#item169329> under a non-exclusive
570 in-perpetuity licence.

571

572

- 573 Aben, F. M., Doan, M.-L., Gratier, J.-P., & Renard, F. (2017, June 30). Coseismic Damage Generation
574 and Pulverization in Fault Zones. *Fault Zone Dynamic Processes*.
575 <https://doi.org/doi:10.1002/9781119156895.ch4>
- 576 Anderson, E. K., Song, W. J., Johnson, S. E., & Cruz-Uribe, A. M. (2021). Mica kink-band geometry as
577 an indicator of coseismic dynamic loading. *Earth and Planetary Science Letters*, 567, 117000.
578 <https://doi.org/https://doi.org/10.1016/j.epsl.2021.117000>
- 579 Aupart, C., Dunkel, K. G., Angheluta, L., Austrheim, H., Ildefonse, B., Malthe-Sørensen, A., &
580 Jamtveit, B. (2018). Olivine Grain Size Distributions in Faults and Shear Zones: Evidence for
581 Nonsteady State Deformation. *Journal of Geophysical Research: Solid Earth*, 123(9), 7421–7443.
582 <https://doi.org/10.1029/2018JB015836>
- 583 Austrheim, H., Dunkel, K. G., Plümpner, O., Ildefonse, B., Liu, Y., & Jamtveit, B. (2017). Fragmentation
584 of wall rock garnets during deep crustal earthquakes. *Science Advances*, 3(2). Retrieved from
585 <http://advances.sciencemag.org/content/3/2/e1602067.abstract>
- 586 Avé Lallemant, H. G. (1978). Experimental deformation of diopside and websterite. *Tectonophysics*,
587 48(1), 1–27. [https://doi.org/https://doi.org/10.1016/0040-1951\(78\)90083-5](https://doi.org/https://doi.org/10.1016/0040-1951(78)90083-5)
- 588 Bestmann, M., Pennacchioni, G., Nielsen, S., Göken, M., & de Wall, H. (2012). Deformation and
589 ultrafine dynamic recrystallization of quartz in pseudotachylyte-bearing brittle faults: A matter
590 of a few seconds. *Journal of Structural Geology*, 38(0), 21–38.
591 <https://doi.org/10.1016/j.jsg.2011.10.001>
- 592 Birtel, S., & Stöckhert, B. (2008). Quartz veins record earthquake-related brittle failure and short
593 term ductile flow in the deep crust. *Tectonophysics*, 457(1–2), 53–63.
594 <https://doi.org/http://dx.doi.org/10.1016/j.tecto.2008.05.018>
- 595 Brückner, L. M., & Trepmann, C. A. (2021). Stresses during pseudotachylyte formation - Evidence
596 from deformed amphibole and quartz in fault rocks from the Silvretta basal thrust (Austria).
597 *Tectonophysics*, 817, 229046. <https://doi.org/https://doi.org/10.1016/j.tecto.2021.229046>
- 598 Brune, J. N. (2001). Fault-normal dynamic unloading and loading: An explanation for "non-gouge"
599 rock powder and lack of fault-parallel shear bands along the San Andreas Fault. In *AGU Fall*
600 *Meeting Abstracts*. San Francisco: AGU.
- 601 Bystricky, M., & Mackwell, S. (2001). Creep of dry clinopyroxene aggregates. *Journal of Geophysical*
602 *Research: Solid Earth*, 106(B7), 13443–13454. <https://doi.org/10.1029/2001JB000333>

603 Campbell, L. R., & Menegon, L. (2019). Transient High Strain Rate During Localized Viscous Creep in
604 the Dry Lower Continental Crust (Lofoten, Norway). *Journal of Geophysical Research: Solid*
605 *Earth*, 124, 10240–10260. <https://doi.org/10.1029/2019JB018052>

606 Campbell, L. R., Menegon, L., Fagereng, & Pennacchioni, G. (2020). Earthquake nucleation in the
607 lower crust by local stress amplification. *Nature Communications*, 11(1), 1322.
608 <https://doi.org/10.1038/s41467-020-15150-x>

609 Campbell, L., Menegon, L. (2021). Electron backscatter diffraction data and sample analysis from the
610 Nusfjord Shear Zone, Lofoten, Norway. NERC EDS National Geoscience Data Centre. (Dataset).
611 <https://doi.org/10.5285/fc332502-1b15-48db-a4f0-16274e924ba0>

612 Corfu, F. (2004). U–Pb Age, Setting and Tectonic Significance of the Anorthosite–Mangerite–
613 Charnockite–Granite Suite, Lofoten–Vesterålen, Norway. *Journal of Petrology*, 45(9), 1799–
614 1819. Retrieved from <http://dx.doi.org/10.1093/petrology/egh034>

615 Doan, M.-L., & Gary, G. (2009). Rock pulverization at high strain rate near the San Andreas fault.
616 *Nature Geoscience*, 2(10), 709–712. <https://doi.org/10.1038/ngeo640>

617 Dohmen, R., Ter heege, J. H., Becker, H.-W., & Chakraborty, S. (2016). Fe-Mg interdiffusion in
618 orthopyroxene. *American Mineralogist*, 101(10), 2210–2221. [https://doi.org/10.2138/am-](https://doi.org/10.2138/am-2016-5815)
619 2016-5815

620 Dor, O., Rockwell, T. K., & Ben-Zion, Y. (2006). Geological Observations of Damage Asymmetry in the
621 Structure of the San Jacinto, San Andreas and Punchbowl Faults in Southern California: A
622 Possible Indicator for Preferred Rupture Propagation Direction. *Pure and Applied Geophysics*,
623 163(2), 301–349. <https://doi.org/10.1007/s00024-005-0023-9>

624 Dorner, D., & Stöckhert, B. (2004). Plastic flow strength of jadeite and diopside investigated by
625 microindentation hardness tests. *Tectonophysics*, 379(1), 227–238.
626 <https://doi.org/https://doi.org/10.1016/j.tecto.2003.11.008>

627 Druiventak, A., Trepmann, C. A., Renner, J., & Hanke, K. (2011). Low-temperature plasticity of olivine
628 during high stress deformation of peridotite at lithospheric conditions — An experimental
629 study. *Earth and Planetary Science Letters*, 311(3), 199–211.
630 <https://doi.org/https://doi.org/10.1016/j.epsl.2011.09.022>

631 Druiventak, A., Matysiak, A., Renner, J., & Trepmann, C. A. (2012). Kick-and-cook experiments on
632 peridotite: simulating coseismic deformation and post-seismic creep. *Terra Nova*, 24(1), 62–69.

633 <https://doi.org/10.1111/j.1365-3121.2011.01038.x>

634 Dunkel, K. G., Zhong, X., Arnestad, P. F., Valen, L. V., & Jamtveit, B. (2020). High transient stress in
635 the lower crust: Evidence from dry pseudotachylytes in granulites, Lofoten Archipelago,
636 northern Norway. *Geology*, *49*(2), 135–139. <https://doi.org/10.1130/G48002.1>

637 Ellis, S., & Stöckhert, B. (2004). Imposed strain localization in the lower crust on seismic timescales.
638 *Earth, Planets and Space*, *56*(12), 1103–1109. <https://doi.org/10.1186/BF03353329>

639 Ferrand, T. P., Hilairet, N., Incel, S., Deldicque, D., Labrousse, L., Gasc, J., et al. (2017). Dehydration-
640 driven stress transfer triggers intermediate-depth earthquakes. *Nature Communications*, *8*,
641 15247. Retrieved from <http://dx.doi.org/10.1038/ncomms15247>

642 Hacker, B. R., Peacock, S. M., Abers, G. A., & Holloway, S. D. (2003). Subduction factory 2. Are
643 intermediate-depth earthquakes in subducting slabs linked to metamorphic dehydration
644 reactions? *Journal of Geophysical Research: Solid Earth*, *108*(B1), 2030.
645 <https://doi.org/10.1029/2001JB001129>

646 Hawemann, F., Mancktelow, N. S., Pennacchioni, G., Wex, S., & Camacho, A. (2019). Weak and Slow,
647 Strong and Fast: How Shear Zones Evolve in a Dry Continental Crust (Musgrave Ranges, Central
648 Australia). *Journal of Geophysical Research: Solid Earth*, *124*(1), 219–240.
649 <https://doi.org/10.1029/2018JB016559>

650 Incel, S., Schubnel, A., Renner, J., John, T., Labrousse, L., Hilairet, N., et al. (2019). Experimental
651 evidence for wall-rock pulverization during dynamic rupture at ultra-high pressure conditions.
652 *Earth and Planetary Science Letters*, *528*, 115832.
653 <https://doi.org/https://doi.org/10.1016/j.epsl.2019.115832>

654 Ingrin, J., Doukhan, N., & Doukhan, J.-C. (1992). Dislocation glide systems in diopside single crystals
655 deformed at 800-900°C. *European Journal of Mineralogy*, *4*(6), 1291–1302.
656 <https://doi.org/10.1127/ejm/4/6/1291>

657 Jamtveit, B., Ben-Zion, Y., Renard, F., & Austrheim, H. (2018). Earthquake-induced transformation of
658 the lower crust. *Nature*, *556*(7702), 487–491. <https://doi.org/10.1038/s41586-018-0045-y>

659 Jamtveit, B., Petley-Ragan, A., Incel, S., Dunkel, K. G., Aupart, C., Austrheim, H., et al. (2019). The
660 Effects of Earthquakes and Fluids on the Metamorphism of the Lower Continental Crust.
661 *Journal of Geophysical Research: Solid Earth*, *0*(0). <https://doi.org/10.1029/2018JB016461>

- 662 Kanagawa, K., Shimano, H., & Hiroi, Y. (2008). Mylonitic deformation of gabbro in the lower crust: A
663 case study from the Pankenushi gabbro in the Hidaka metamorphic belt of central Hokkaido,
664 Japan. *Journal of Structural Geology*, 30(9), 1150–1166.
665 <https://doi.org/https://doi.org/10.1016/j.jsg.2008.05.007>
- 666 Keulen, N., Heilbronner, R., Stünitz, H., Boullier, A.-M. M., & Ito, H. (2007). Grain size distributions of
667 fault rocks: A comparison between experimentally and naturally deformed granitoids. *Journal*
668 *of Structural Geology*, 29(8), 1282–1300.
669 <https://doi.org/http://dx.doi.org/10.1016/j.jsg.2007.04.003>
- 670 Kirby, S. H., & Kronenberg, A. K. (1984). Deformation of clinopyroxenite: Evidence for a transition in
671 flow mechanisms and semibrittle behavior. *Journal of Geophysical Research: Solid Earth*,
672 89(B5), 3177–3192. <https://doi.org/10.1029/JB089iB05p03177>
- 673 Kohlstedt, D. L., & Vander Sande, J. B. (1973). Transmission electron microscopy investigation of the
674 defect microstructure of four natural orthopyroxenes. *Contributions to Mineralogy and*
675 *Petrology*, 42(2), 169–180. <https://doi.org/10.1007/BF00371506>
- 676 Kollé, J. J., & Blacic, J. D. (1982). Deformation of single-crystal clinopyroxenes: 1. Mechanical
677 twinning in diopside and hedenbergite. *Journal of Geophysical Research: Solid Earth*, 87(B5),
678 4019–4034. <https://doi.org/10.1029/JB087iB05p04019>
- 679 Kollé, J. J., & Blacic, J. D. (1983). Deformation of single-crystal clinopyroxenes: 2. Dislocation-
680 controlled flow processes in Hedenbergite. *Journal of Geophysical Research: Solid Earth*,
681 88(B3), 2381–2393. <https://doi.org/10.1029/JB088iB03p02381>
- 682 Lloyd, G. E., Farmer, A. B., & Mainprice, D. (1997). Misorientation analysis and the formation and
683 orientation of subgrain and grain boundaries. *Tectonophysics*, 279(1), 55–78.
684 [https://doi.org/https://doi.org/10.1016/S0040-1951\(97\)00115-7](https://doi.org/https://doi.org/10.1016/S0040-1951(97)00115-7)
- 685 Markl, G., Frost, B. R., & Bucher, K. (1998). The Origin of Anorthosites and Related Rocks from the
686 Lofoten Islands, Northern Norway: I. Field Relations and Estimation of Intrinsic Variables.
687 *Journal of Petrology*, 39(8), 1425–1452. <https://doi.org/10.1093/petroj/39.8.1425>
- 688 Matysiak, A. K., & Trepmann, C. A. (2012). Crystal–plastic deformation and recrystallization of
689 peridotite controlled by the seismic cycle. *Tectonophysics*, 530–531, 111–127.
690 <https://doi.org/https://doi.org/10.1016/j.tecto.2011.11.029>
- 691 Menegon, L., Pennacchioni, G., Malaspina, N., Harris, K., & Wood, E. (2017). Earthquakes as
692 Precursors of Ductile Shear Zones in the Dry and Strong Lower Crust. *Geochemistry*,

693 *Geophysics, Geosystems*, 18(12), 4356–4374. <https://doi.org/10.1002/2017GC007189>

694 Milke, R., Neusser, G., Kolzer, K., & Wunder, B. (2013). Very little water is necessary to make a dry
695 solid silicate system wet. *Geology*, 41(2), 247–250. <https://doi.org/10.1130/G33674.1>

696 Ngo, D., Huang, Y., Rosakis, A., Griffith, W. A., & Pollard, D. (2012). Off-fault tensile cracks: A link
697 between geological fault observations, lab experiments, and dynamic rupture models. *Journal*
698 *of Geophysical Research: Solid Earth*, 117(B1), B01307. <https://doi.org/10.1029/2011jb008577>

699 Okudaira, T., Jeřábek, P., Stünitz, H., & Fousseis, F. (2015). High-temperature fracturing and
700 subsequent grain-size-sensitive creep in lower crustal gabbros: Evidence for coseismic loading
701 followed by creep during decaying stress in the lower crust? *Journal of Geophysical Research:*
702 *Solid Earth*, 120(5), 3119–3141. <https://doi.org/10.1002/2014JB011708>

703 Orlandini, O. F., & Mahan, K. H. (2020). Rheological evolution of a pseudotachylyte-bearing deep
704 crustal shear zone in the western Canadian shield. *Journal of Structural Geology*, 141, 104188.
705 <https://doi.org/https://doi.org/10.1016/j.jsg.2020.104188>

706 Papa, S., Pennacchioni, G., Angel, R. J., & Faccenda, M. (2018). The fate of garnet during (deep-
707 seated) coseismic frictional heating: The role of thermal shock. *Geology*, 46(5), 471–474.
708 <https://doi.org/10.1130/G40077.1>

709 Papa, S., Pennacchioni, G., Menegon, L., & Thielmann, M. (2020). High-stress creep preceding
710 coseismic rupturing in amphibolite-facies ultramylonites. *Earth and Planetary Science Letters*,
711 541, 116260. <https://doi.org/https://doi.org/10.1016/j.epsl.2020.116260>

712 Petley-Ragan, A., Dunkel, K. G., Austrheim, H., Ildefonse, B., & Jamtveit, B. (2018). Microstructural
713 Records of Earthquakes in the Lower Crust and Associated Fluid-Driven Metamorphism in
714 Plagioclase-Rich Granulites. *Journal of Geophysical Research: Solid Earth*, 123(5), 3729–3746.
715 <https://doi.org/10.1029/2017JB015348>

716 Petley-Ragan, A., Ben-Zion, Y., Austrheim, H., Ildefonse, B., Renard, F., & Jamtveit, B. (2019).
717 Dynamic earthquake rupture in the lower crust. *Science Advances*, 5(7), eaaw0913.
718 <https://doi.org/10.1126/sciadv.aaw0913>

719 Petley-Ragan, A. J., Plümper, O., Ildefonse, B., and Jamtveit, B.: Nanoscale earthquake records
720 preserved in plagioclase microfractures from the lower continental crust, *Solid Earth*, 12, 959–
721 969, <https://doi.org/10.5194/se-12-959-2021>, 2021

722 Raleigh, C. B., & Talbot, J. L. (1967). Mechanical twinning in naturally and experimentally deformed

723 diopside. *American Journal of Science*, 265(2), 151–165. <https://doi.org/10.2475/ajs.265.2.151>

724 Reches, Z., & Dewers, T. A. (2005). Gouge formation by dynamic pulverization during earthquake
725 rupture. *Earth and Planetary Science Letters*, 235(1), 361–374.
726 <https://doi.org/https://doi.org/10.1016/j.epsl.2005.04.009>

727 Sammis, C. G., Osborne, R. H., Anderson, J. L., Banerdt, M., & White, P. (1986). Self-similar cataclasis
728 in the formation of fault gouge. *Pure and Applied Geophysics*, 124(1), 53–78.
729 <https://doi.org/10.1007/BF00875719>

730 Sibson, R. H., & Toy, V. G. (2006). The habitat of fault-generated pseudotachylite: Presence vs.
731 absence of friction-melt. In *Earthquakes: Radiated Energy and the Physics of Faulting* (Vol. 170,
732 pp. 153–166). Washington, DC: AGU. <https://doi.org/10.1029/170GM16>

733 Skemer, P., & Karato, S. (2007). Effects of solute segregation on the grain-growth kinetics of
734 orthopyroxene with implications for the deformation of the upper mantle. *Physics of the Earth
735 and Planetary Interiors*, 164(3), 186–196.
736 <https://doi.org/https://doi.org/10.1016/j.pepi.2007.06.011>

737 Soda, Y., & Okudaira, T. (2018). Microstructural evidence for the deep pulverization in a lower crustal
738 meta-anorthosite. *Terra Nova*, 30(6), 399–405. <https://doi.org/10.1111/ter.12355>

739 Song, B. R., Johnson, S. E., Song, W. J., Gerbi, C. C., & Yates, M. G. (2020). Coseismic damage runs
740 deep in continental strike-slip faults. *Earth and Planetary Science Letters*, 539, 116226.
741 <https://doi.org/https://doi.org/10.1016/j.epsl.2020.116226>

742 Stünitz, Holger, Keulen, N., Hirose, T., & Heilbronner, R. (2010). Grain size distribution and
743 microstructures of experimentally sheared granitoid gouge at coseismic slip rates – Criteria to
744 distinguish seismic and aseismic faults? *Journal of Structural Geology*, 32(1), 59–69.
745 <https://doi.org/http://dx.doi.org/10.1016/j.jsg.2009.08.002>

746 Sullivan, W. A., & Peterman, E. M. (2017). Pulverized granite at the brittle-ductile transition: An
747 example from the Kellyland fault zone, eastern Maine, U.S.A. *Journal of Structural Geology*,
748 101, 109–123. <https://doi.org/https://doi.org/10.1016/j.jsg.2017.07.002>

749 Trepmann, C. A., & Stöckhert, B. (2013). Short-wavelength undulatory extinction in quartz recording
750 coseismic deformation in the middle crust; An experimental study. *Solid Earth*, 4(2), 263–276.
751 <https://doi.org/10.5194/se-4-263-2013>

752 Trepmann, C. A., Renner, J., & Druiventak, A. (2013). Experimental deformation and recrystallization

- 753 of olivine-processes and timescales of damage healing during postseismic relaxation at mantle
754 depths. *Solid Earth*, 4(2), 423–450. <https://doi.org/10.5194/se-4-423-2013>
- 755 Trepmann, C. A., & Seybold, L. (2019). Deformation at low and high stress-loading rates. *Geoscience*
756 *Frontiers*, 10(1), 43–54. <https://doi.org/https://doi.org/10.1016/j.gsf.2018.05.002>
- 757 Trepmann, Claudia A, & Stöckhert, B. (2002). Cataclastic deformation of garnet: a record of
758 synseismic loading and postseismic creep. *Journal of Structural Geology*, 24(11), 1845–1856.
759 [https://doi.org/https://doi.org/10.1016/S0191-8141\(02\)00004-4](https://doi.org/https://doi.org/10.1016/S0191-8141(02)00004-4)
- 760 Wilson, B., Dewers, T., Reches, Z., & Brune, J. (2005). Particle size and energetics of gouge from
761 earthquake rupture zones. *Nature*, 434(7034), 749–752. <https://doi.org/10.1038/nature03433>
- 762 Xu, S., & Ben-Zion, Y. (2017). Theoretical constraints on dynamic pulverization of fault zone rocks.
763 *Geophysical Journal International*, 209(1), 282–296. <https://doi.org/10.1093/gji/ggx033>
- 764 Yuan, F., Prakash, V., & Tullis, T. (2011). Origin of pulverized rocks during earthquake fault rupture.
765 *Journal of Geophysical Research: Solid Earth*, 116(B6). <https://doi.org/10.1029/2010JB007721>